






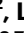



XENTURION is a population-level multidimensional resource of xenografts and tumoroids from metastatic colorectal cancer patients

Received: 26 April 2023

Accepted: 19 August 2024

Published online: 29 August 2024

 Check for updates


Simonetta M. Leto ^{1,6}, Elena Grassi ^{1,2,6}, Marco Avolio^{1,2}, Valentina Vurchio^{1,2}, Francesca Cottino¹, Martina Ferri^{1,2}, Eugenia R. Zanella¹, Sofia Borgato^{1,2}, Giorgio Corti ², Laura di Blasio ^{1,2}, Desiana Somale^{1,4}, Marianela Vara-Messler^{1,2,5}, Francesco Galimi^{1,2}, Francesco Sassi¹, Barbara Lupo^{1,2}, Irene Catalano¹, Marika Pinnelli^{1,2}, Marco Viviani ^{1,2}, Luca Sperti^{1,2}, Alfredo Mellano¹, Alessandro Ferrero³, Caterina C. Zingaretti³, Alberto Puliafito^{1,2}, Luca Primo ^{1,2}, Andrea Bertotti^{1,2,7}  & Livio Trusolino ^{1,2,7} 

The breadth and depth at which cancer models are interrogated contribute to the successful clinical translation of drug discovery efforts. In colorectal cancer (CRC), model availability is limited by a dearth of large-scale collections of patient-derived xenografts (PDXs) and paired tumoroids from metastatic disease, where experimental therapies are typically tested. Here we introduce XENTURION, an open-science resource offering a platform of 128 PDX models from patients with metastatic CRC, along with matched PDX-derived tumoroids. Multidimensional omics analyses indicate that tumoroids retain extensive molecular fidelity with parental PDXs. A tumoroid-based trial with the anti-EGFR antibody cetuximab reveals variable sensitivities that are consistent with clinical response biomarkers, mirror tumor growth changes in matched PDXs, and recapitulate *EGFR* genetic deletion outcomes. Inhibition of adaptive signals upregulated by EGFR blockade increases the magnitude of cetuximab response. These findings illustrate the potential of large living biobanks, providing avenues for molecularly informed preclinical research in oncology.

The initial development of cancer organoids, or tumoroids, from CRC samples¹ has paved the way for the establishment of living biobanks across various tumor types^{2,3}. While this technology has contributed to improving precision medicine in CRC^{4–6}, its long-term impact has not met expectations in terms of the numbers of models generated, extent

and depth of molecular profiling, clinical representativeness, and value in predicting therapeutic response at the population level. Existing CRC tumoroid platforms typically include fewer than a hundred samples. The composition of existing catalogs further decreases to the order of tens when considering the availability of accompanying

¹Candiolo Cancer Institute – FPO IRCCS, Candiolo, Torino, Italy. ²Department of Oncology, University of Torino, Candiolo, Torino, Italy. ³Mauriziano Umberto I Hospital, Torino, Italy. ⁴Present address: Aptuit, an Evotec Company, Verona, Italy. ⁵Present address: Sanofi Belgium, Zwiinaarde, Belgium. ⁶These authors contributed equally: Simonetta M. Leto, Elena Grassi. ⁷These authors jointly supervised this work: Andrea Bertotti and Livio Trusolino.

 e-mail: andrea.bertotti@ircc.it; livio.trusolino@ircc.it

molecular and pharmacologic information, and only a handful of models have matched PDX counterparts for running companion in vivo studies^{7,8}. Owing to this paucity of cases, current biobanks of CRC tumoroids have important limitations: i) they often fail to capture intertumor diversity, which weakens the predictive power of regression models when trying to extract subgroup-defined genotype/phenotype associations; ii) they hardly contemplate systematic in vivo validation with paired xenografts, which diminishes the informative value of tumoroid-based drug development pipelines; iii) small sample size also complicates methodological work, such as assessing whether tumoroid establishment is biased by biological traits in originating tumors that influence cell culture viability.

Another challenge to the clinical transferability of drug screen approaches using CRC tumoroids is that, with some exceptions^{9–12}, pharmacologic experiments have typically been conducted in cultures established from colon primary tumor samples of treatment-naïve patients. While these tumoroid models are valuable for biological investigation and target discovery, their response to drug perturbations may differ from that of tumoroids from patients exposed to prior anticancer therapy. This potential discrepancy can lead to attrition in drug development, as investigational compounds that enter the clinical space after successful preclinical testing are almost invariably administered to heavily pretreated metastatic patients. Finally, there is growing appreciation of the importance of standardizing practices and protocols to enhance reproducibility¹³. This need calls for ordered procedural attempts to optimize culture conditions, validate source characteristics, and define the most reliable measures of effects and the most accurate endpoint methodologies.

To tackle some of these hurdles we have developed XENTURION, a resource of matched XENografts and Tumoroids for Research In ONcology that encompasses 128 sibling pairs of PDXs and PDX-derived tumoroids (PDXTs) from patients with metastatic CRC. The vast majority of XENTURION models underwent comparative analysis at the mutational, gene copy number and transcriptomic levels and were annotated for response to the clinically approved anti-EGFR antibody cetuximab ex vivo and in vivo, showing substantial consistency in all the data levels examined. Further, we embarked on a proof-of-principle discovery effort to identify and prioritize druggable co-extinction targets, and found that inhibition of top candidates increased the depth of response to cetuximab. This platform addresses a long-standing quest for large-scale collections of extensively annotated CRC preclinical models for integrative ex vivo and in vivo preclinical applications. All molecular profiles and therapeutic annotations are accessible in public repositories and as Supplementary Data here, and models are available for distribution to non-profit entities. By accessing XENTURION, the biomedical community will gain access to a comprehensive knowledge base of disseminatable methods, resources, and information to streamline preclinical studies and accelerate the development of additional treatments for patients with advanced CRC.

Results

Facts and figures of XENTURION

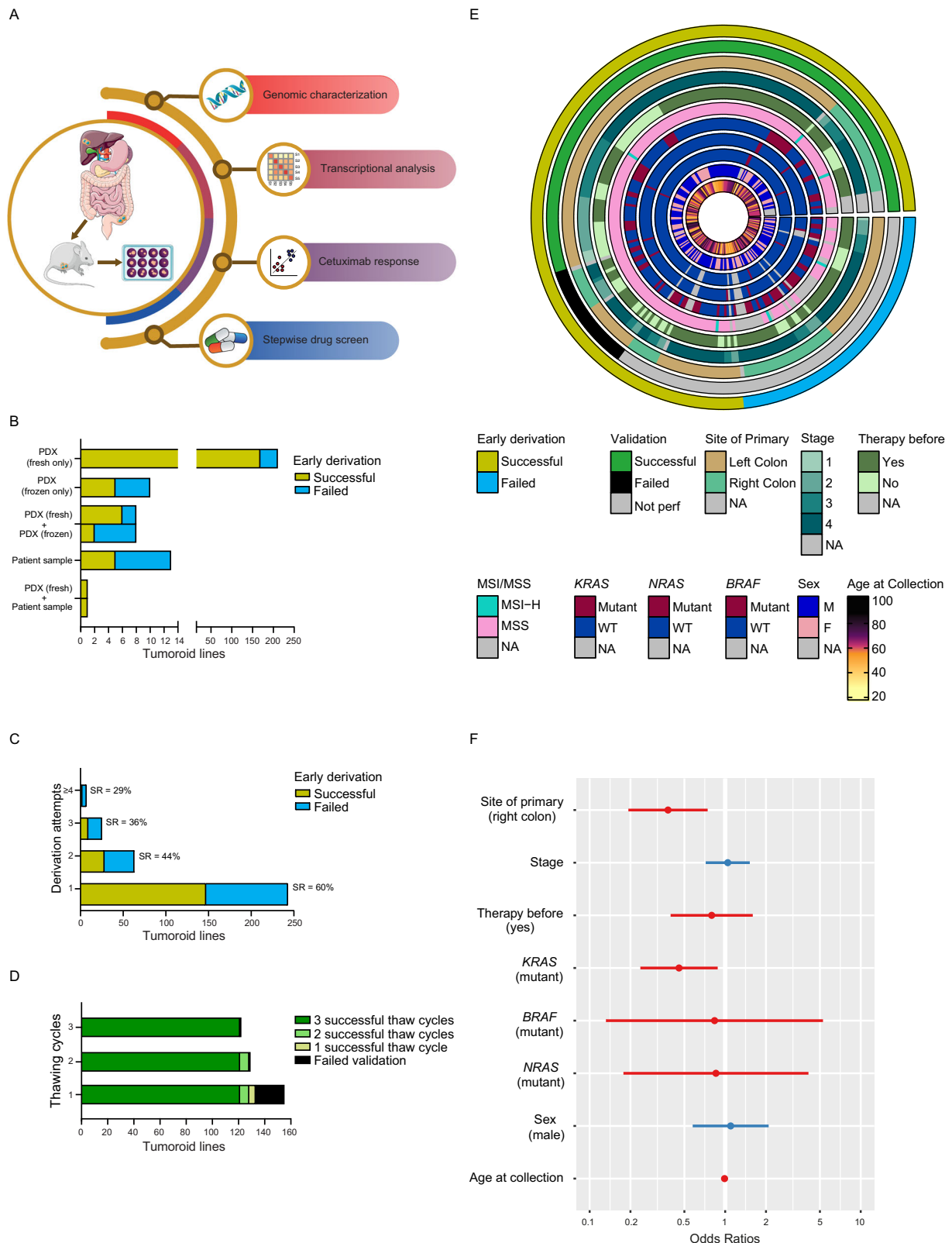
PDXs provide a nearly unlimited source of high-quality, propagatable material for generating ex vivo preclinical models. Drawing on our experience with PDX establishment and characterization^{14–18}, we have created a biobank of matched PDXs and PDXTs that reflects the biological and clinical diversity of metastatic CRC. The primary purpose of this biobank is to streamline the identification, screening, and prioritization of anticancer agents in the preclinical development pipeline to expedite the selection process before embarking on more resource-intensive in vivo validations. While the characterization of CRC tumoroid collections derived directly from patient tumors is extensive^{1,4,9–12}, limited information exists regarding the molecular and biological fidelity of PDXTs. To address this knowledge gap, we performed a systematic comparison between paired PDXs and PDXTs in

terms of mutational profiles, gene copy number architecture, transcriptomic features, and responsiveness to standard-of-care therapy. This comparative effort was also leveraged to extract genes that exhibited concordant modulation under drug pressure in both PDXs and PDXTs, with the aim to pinpoint hits potentially involved in tumor adaptation to therapeutic stress. Following hit nomination, a stepwise drug screen for actionable targets was conducted in PDXTs, and surviving candidate compounds were finally tested in vivo. The workflow of XENTURION characterization is illustrated in Fig. 1A.

Between March 2015 and September 2021, a total of 267 CRC liver metastases from 260 patients were processed for tumoroid derivation (for seven cases, two liver metastases from the same patient were available). Information on treatment history was accessible for 255 donor patients (Supplementary Data 1). Of these patients, 174 (68.2%) had received prior chemotherapy. Treatments included an oxaliplatin-based regimen ($n = 117$, 45.9%), an irinotecan-based regimen ($n = 34$, 13.3%), a sequential or combination therapy with both oxaliplatin and irinotecan ($n = 20$, 7.8%), or capecitabine alone ($n = 3$, 1.18%). Chemotherapy was administered together with targeted agents (the anti-EGFR antibodies cetuximab or panitumumab and/or the anti-VEGFA antibody bevacizumab) in 85 patients (33.3%).

To minimize alterations in the biology of tumors and prevent biased selection of specific growth dependencies, we standardized culture conditions that sustained long-term growth of tumoroids in a minimal medium containing EGF as the sole exogenous growth factor. The chosen EGF concentration (20 ng/ml) was adjusted to secure tumoroid proliferation on a population scale. This approach draws inspiration from previous work aimed at defining optimal culture conditions for human and mouse CRC tumoroids^{19,20} and aligns with the notion that CRC tumoroids gradually become independent from niche signals during cancer progression²¹. For preliminary inclusion into the biobank, each PDX-tumoroid pair had to show matching identity with the original material by genetic fingerprinting, negativity for human and mouse pathogens, and a histology congruent with CRC phenotypes. This approach resulted in the inclusion of 243 models; 19 cases were excluded due to discordant DNA fingerprinting between the PDX-tumoroid pairs and the original patient sample (see Methods); four were diagnosed as lymphomas by histopathological evaluation; and one was excluded for technical reasons (deterioration of archived material) (Supplementary Data 2).

We categorized tumoroids as ‘early-stage’ when their initial propagation cultures could be expanded to a minimum of 200,000 viable cells for cryopreservation, typically achieved after three rounds of cell splitting. The vast majority of samples (211/243, 87%) were processed using freshly explanted PDX tumors as the only source, achieving an 80% success rate (169/211) (Fig. 1B and Supplementary Data 2). In the few instances where PDXT derivation was attempted from frozen PDX tumors, the success rate was lower (5/10, 50%) (Fig. 1B and Supplementary Data 2). Differences in the generation of early-stage PDXTs were also evident when tumoroids were derived in parallel from fresh and frozen material from the same PDX; in particular, among eight PDXs with both fresh and frozen tumor fragments available, early-stage PDXTs were successfully established solely from fresh tissues in four cases and from both fresh and frozen tissues in two cases, resulting in an overall success rate of 75% (6/8) for fresh explants and 25% (2/8) for frozen material (Fig. 1B and Supplementary Data 2). Although the number of early-stage PDXTs from frozen PDX tumors is limited, these findings suggest that freshly explanted tumors may be more conducive to PDXT initial propagation than frozen material. XENTURION also includes 13 tumoroids directly derived from fresh human specimens after surgery; in this subgroup, the success rate in the production of early-stage tumoroids was markedly lower (5/13, 38%). Finally, for one case, early-stage tumoroids were successfully obtained from both fresh PDX explants and the original patient sample (Fig. 1B and Supplementary Data 2).



Overall, XENTURION comprises 186 early-stage tumoroids of metastatic CRC, with a success rate of 77% (186/243); the collection is predominantly represented by PDX lines (181/186, 97%), each with paired PDXs available (Fig. 1B and Supplementary Data 2). In most models, a single derivation procedure sufficed to yield early-stage tumoroids, with a success rate of 60% (147/243) (Fig. 1C). In cases where early-stage tumoroid establishment failed after the first

attempt, two or more additional rounds were performed if PDXs were available. The success rate of early-stage tumoroid establishment showed a proportional decrease with attempt repetition: 44% after the second attempt, 36% after the third attempt, and 29% after the fourth or subsequent attempts (Fig. 1C). Hence, we can reasonably conclude that tumoroids of metastatic CRC that do not grow in culture after the first derivation round are less likely to give rise to early-stage models.

Fig. 1 | Facts and figures of XENTURION. **A** Schematic overview of XENTURION experimental design. Matched PDXTs and PDXs were subjected to comparative mutational, gene copy number and transcriptomic analyses. Molecular annotation was paralleled by systematic assessment of *ex vivo* and *in vivo* response to cetuximab. Post-cetuximab transcriptomic profiles were leveraged to extract upregulated genes potentially involved in adaptive resistance to EGFR blockade. Compounds against candidate targets were tested in a stepwise drug screen, and those that proved effective in PDXT assays underwent final validation in PDXs. **B, C** Success rate in the early derivation of tumoroid lines according to the nature of the sample of origin (**B**) or the number of derivation attempts (**C**). When early-stage tumoroids were derived from different originating samples (e.g., fresh and frozen PDX explants), success rates were computed for models derived from freshly explanted tumors. SR success rate. **D** Number of validated tumoroids according to the number of freeze-thaw cycles. **E** Main clinical and molecular features of the starting population from which tumoroid derivation was attempted. The circus plot

includes all quality-checked cases with successful validation ($n = 133$), those that failed validation ($n = 24$), early-stage cases for which validation was not performed (Not perf, $n = 29$), and those that failed early derivation ($n = 57$). F female, M male, MSI-H microsatellite instability high, MSS microsatellite stability, NA not available, WT wild-type. **F** Odds ratios of a multivariate logistic regression with success status of PDXT early derivation and validation (1, successful, $n = 129$; 0, failed, $n = 73$) as dependent variable and several clinical and molecular annotations as independent variables. Red color indicates that the independent variable has a negative effect on the validation rate; blue color indicates the opposite. The only continuous variables are stage and age at collection; all other variables are binary. Confidence interval of odds ratios, 95%. Panel **A** was partly generated using adaptations of open-access pictures released under Creative Commons Attribution Licenses; see Figure preparation in the Methods for credits and details. Source data are provided as a Source Data file.

To qualify as validated models capable of long-term recovery and expansion, early-stage tumoroids underwent a minimum of three freeze-thaw cycles. DNA fingerprinting-based identity checks and microbiologic tests for Mycoplasma detection were conducted after each cycle. Of the 145 early-stage tumoroids subjected to at least three freeze-thaw cycles, 121 (83%) passed validation (Fig. 1D and Supplementary Data 2). Notably, the lack of recovery after the first freeze-thaw cycle proved to be a reliable indicator, identifying 92% (22/24) of cases that would not withstand additional ‘rescue’ cycles and, therefore, would fail validation. Conversely, almost all early-stage tumoroids that successfully recovered after the first freeze-thaw cycle proceeded to complete validation in subsequent cycles (121/123, 98.37%) (Fig. 1D and Supplementary Data 2). For this reason, we admitted in the final collection of validated cases additional models that had survived two freeze-thaw cycles (seven cases) or one cycle (five cases).

Based on these selection criteria, an initial version of the collection encompassed a total of 133 validated tumoroids: 129 PDXTs (with paired PDXs) and four tumoroids directly derived from donor patients (Fig. 1D and Supplementary Data 2). PDXTs and their matched PDXs with sufficient and good-quality nucleic acid material were processed to obtain mutational, gene copy number and transcriptomic profiles. Of note, one validated PDXT model was identified as an anal squamous cell carcinoma after subsequent transcriptomic analysis and post hoc pathological examination. Therefore, the final count of the definitive XENTURION collection comprises a total of 128 fully validated PDX/PDXT pairs, with a complete dataset for all molecular dimensions available for 114 paired siblings.

The key clinical and molecular attributes of the samples that fed into XENTURION, including primary tumor sidedness and stage, patients’ sex, age and exposure to therapy before sample donation, DNA microsatellite status, and the presence of clinically relevant driver mutations, are summarized in Fig. 1E. To explore whether the process of tumoroid derivation led to over- or under-representation of these features in XENTURION compared to the starting population, we assessed their relative distribution in validated models versus those failing early-stage derivation or validation. Enrichment analysis revealed that early-stage derivation or validation of metastatic samples with primary tumor location in the right colon was less successful than expected by chance ($P = 0.005$, odds ratio [OR] = 0.38, 95% confidence interval [CI] 0.19–0.74) (Fig. 1F). This observation may be attributed to the fact that left-sided CRC tumors, which are usually more dependent on EGFR signaling²², were more stimulated to grow in the presence of the EGF ligand present in the culture medium compared to right-sided tumors. A similar enrichment among samples that failed to be established was observed for tumors harboring *KRAS* mutations ($P = 0.019$, OR = 0.46, 95% CI 0.23–0.88) (Fig. 1F). This result was unexpected, given that *KRAS* mutant CRC tumors are generally more aggressive than *KRAS* wild-type tumors^{23,24}, and ectopic introduction of mutant *KRAS* promotes – rather than contrasts – the expansion of CRC

tumoroids²⁵. We suspected that the higher representation of *KRAS* mutant cases among tumoroids that did not survive initial derivation or validation might be related to a procedural bias linked to the timing of tumoroid generation. Indeed, PDXTs from *KRAS* wild-type tumors were more often derived from late-passage (more than three) PDXs, typically from large cohorts propagated *in vivo* multiple times to obtain sufficient replicas for testing with the anti-EGFR antibody cetuximab. Since mutant *KRAS* confers resistance to cetuximab²⁶, PDXs with *KRAS* mutations were not repeatedly expanded for cetuximab treatment, and tumoroids were more frequently generated from smaller cohorts at earlier passages. To test this hypothesis, we computed the PDX passage at which tumoroids were derived along with the two significant enrichments shown in Fig. 1F (*KRAS* mutations and tumor right-sidedness) using logistic regression. In multivariate analysis, the odds ratio of tumor sidedness maintained statistical significance ($P = 0.025$, OR = 0.32, 95% CI 0.12–0.86), whereas the odds ratio of *KRAS* mutations became not significant ($P = 0.313$, OR = 0.64, 95% CI 0.26–1.53) (Supplementary Fig. 1). Accordingly, there was a trend for late-passage PDXs to be more likely to yield validated tumoroids than early-passage PDXs ($P = 0.097$, OR = 1.29, 95% CI 0.97–1.76) (Supplementary Fig. 1). This supports the assumption that PDX passaging rather than *KRAS* mutations impacted PDXT stability. This observation is in line with our finding that fresh samples from patients (never passaged in mice) were less susceptible to grow in culture (Fig. 1B), suggesting that serial mouse engraftment eases the adaptation of cancer cells to long-term propagation *ex vivo*.

Mutational and gene copy number analysis of paired PDXTs and PDXs reveals substantial model concordance

We performed targeted next-generation sequencing of 116 relevant CRC genes²⁷ to detect small somatic alterations (single nucleotide variants [SNVs] and indels) in a set of 125 sibling pairs comprising validated PDXTs and matched PDXs with sufficient and good-quality DNA material. The overall distribution of variant allele frequencies (VAFs) and the number of identified variants showed consistency between PDXTs and PDXs ($P = 0.09$ and $P = 0.72$, respectively, by Kolmogorov-Smirnov test) (Supplementary Fig. 2). At the level of individual genes, the vast majority of mutations were conserved (Fig. 2A). A statistically significant imbalance, with a higher representation of gene mutations in PDXTs, was observed only for *APC* ($P = 0.021$ by χ^2 test) and *KAT6A* ($P = 0.046$ by χ^2 test). However, manual curation of sequencing reads confirmed the presence of *APC* and *KAT6A* mutations in 21/24 (87.5%) and 4/6 (66.7%) of the corresponding PDXs, respectively (Supplementary Fig. 3). The overall consistency of the mutational landscape between the PDX-PDXT pairs extended to the level of specific mutations. The Jaccard similarity coefficient, used to quantify this concordance, was markedly higher for matched models than unmatched models (median matched, 1.00, interquartile range [IQR] 0.66–1.00; median unmatched, 0.00, IQR 0.00–0.00;

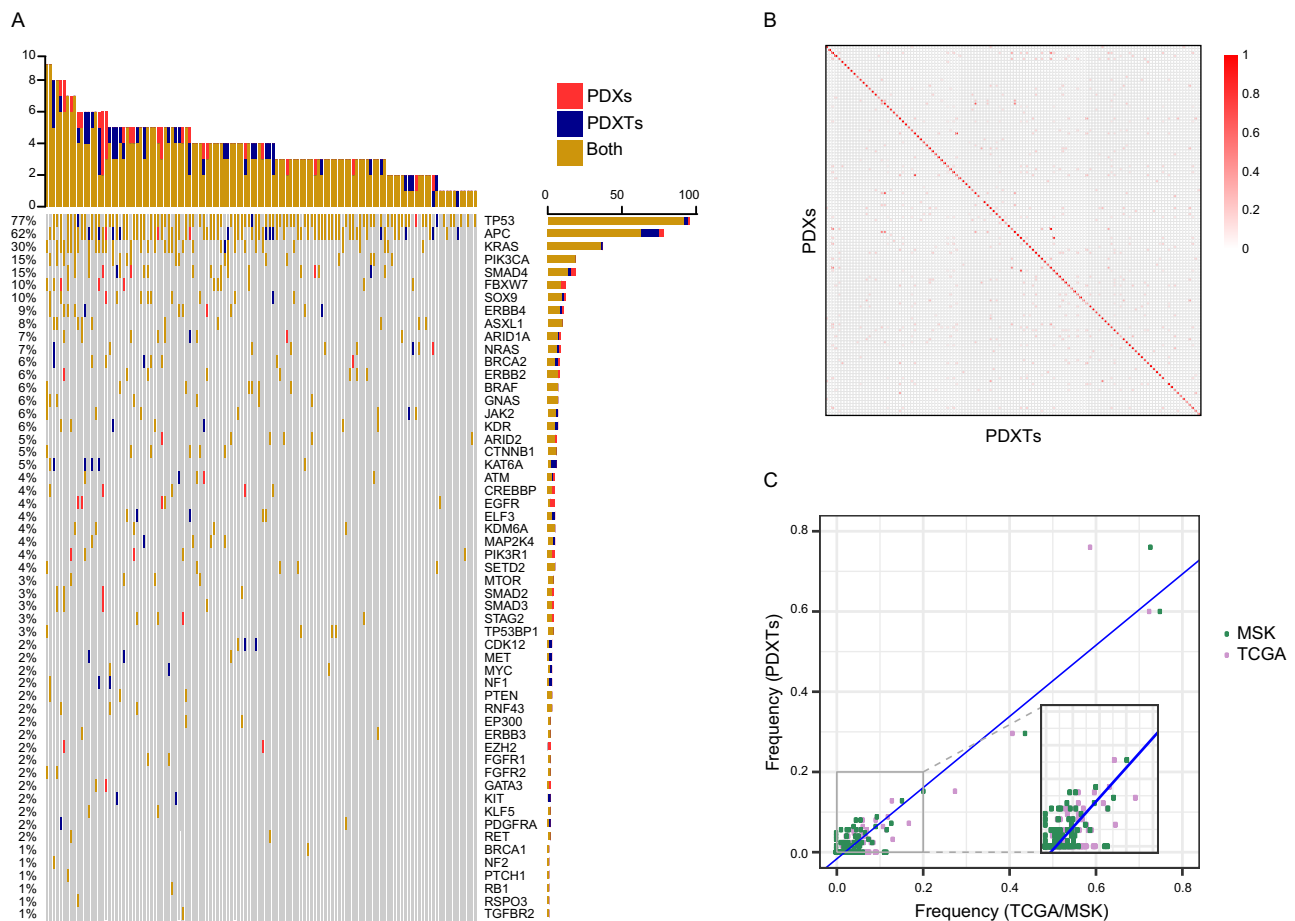


Fig. 2 | Comparative landscape of somatic single nucleotide variations and indels in paired PDXTs and PDXs. A Common and private alterations in 124 pairs of matched PDXTs and PDXs. One pair for which mutational data were available was excluded because no alterations with VAFs > 0.05 were detected. Genes without any alteration in the whole cohort were removed. The top barchart shows the total number of mutations for each sample. The barchart on the right shows the

percentage of mutations for each gene in the cohort. **B** Jaccard similarity indexes of somatic alterations between 124 matched PDXs and PDXTs. **C** Gene-level population frequencies of mutational alterations in PDXTs versus those detected in the TCGA dataset or the MSK-IMPACT dataset; the inset shows that the correlation is not driven solely by genes with high mutational frequencies. Source data are provided as a Source Data file.

$P < 2.2 \times 10^{-308}$ by two-tailed Mann–Whitney test) (Fig. 2B). Importantly, the extent of mutational concordance between PDXTs and PDXs mirrored that of a recent comparison involving 536 original patient tumors and matched PDXs across 25 cancer types²⁸. This indicates negligible divergence between pre-derivation samples, PDXs and PDXTs when considering the general mutational repertoire.

Subclonal variants that are poorly represented in PDXs may become dominant in PDXTs if they confer a growth advantage in culture. To study the clonal composition of PDX–PDXT pairs, we examined the prevalence of shared mutations with VAFs higher than 0.05 for genes with at least five alterations in the collection. No significant differences in allele frequencies emerged from this analysis ($P = 0.66$ by paired t -test) (Supplementary Figs. 4 and 5), indicating that intratumor clonal heterogeneity was substantially preserved in PDXTs with respect to originating PDXs. In some cases, the allele frequencies of alterations in frequently mutated tumor suppressor genes (for example, *APC* and *TP53*) were 1 in PDXTs and slightly lower in the paired xenografts (Supplementary Fig. 4), suggesting subtle defects in the filtering procedure of mouse reads deriving from host stromal contamination.

Next, we compared the frequency of gene alterations in our collection with two large datasets of human samples from CRC patients: TCGA, mainly consisting of primary tumors²⁷, and MSK-IMPACT, predominantly composed of metastatic samples²⁹. We found significant

correlations between PDXTs and both clinical datasets (Pearson coefficient, 0.93, $P = 1.46 \times 10^{-51}$ for TCGA; Pearson coefficient, 0.96, $P = 2.37 \times 10^{-64}$ for MSK-IMPACT) (Fig. 2C) as well as between PDXs and these datasets (Pearson coefficient, 0.92, $P = 4.24 \times 10^{-49}$ for TCGA and 0.95, $P = 4.57 \times 10^{-62}$ for MSK-IMPACT) (Supplementary Fig. 6). It is worth noting that colorectal tumors with microsatellite instability (MSI) are typically less prevalent in metastases compared to primary tumors, consistent with their generally better prognosis³⁰. For example, MSI tumors account for approximately 12% of cases in the TCGA dataset of primary tumors²⁷, 4% in the MSK-IMPACT collection of metastatic lesions²⁹, and 2.46% (6/243) in XENTURION metastatic PDXs (Fig. 1E). Despite this difference, the above comparisons underscore that XENTURION reflects the overall mutational landscape of patient cohorts and point to substantial similarity in mutational frequencies between primary and metastatic CRC tumors. A high level of genomic concordance between primary and metastatic colorectal tumors has already been documented in an MSK-IMPACT comparative analysis of recurrently mutated genes²⁹.

We then investigated whether the PDXT validation protocol could lead to the enrichment or depletion of defined variants. By applying univariate logistic regression models to predict validation, we considered the presence or absence of any SNVs or indels in PDXTs as independent variables and the validation status as the dependent variable. Among genes mutated in at least five tumoroids, only

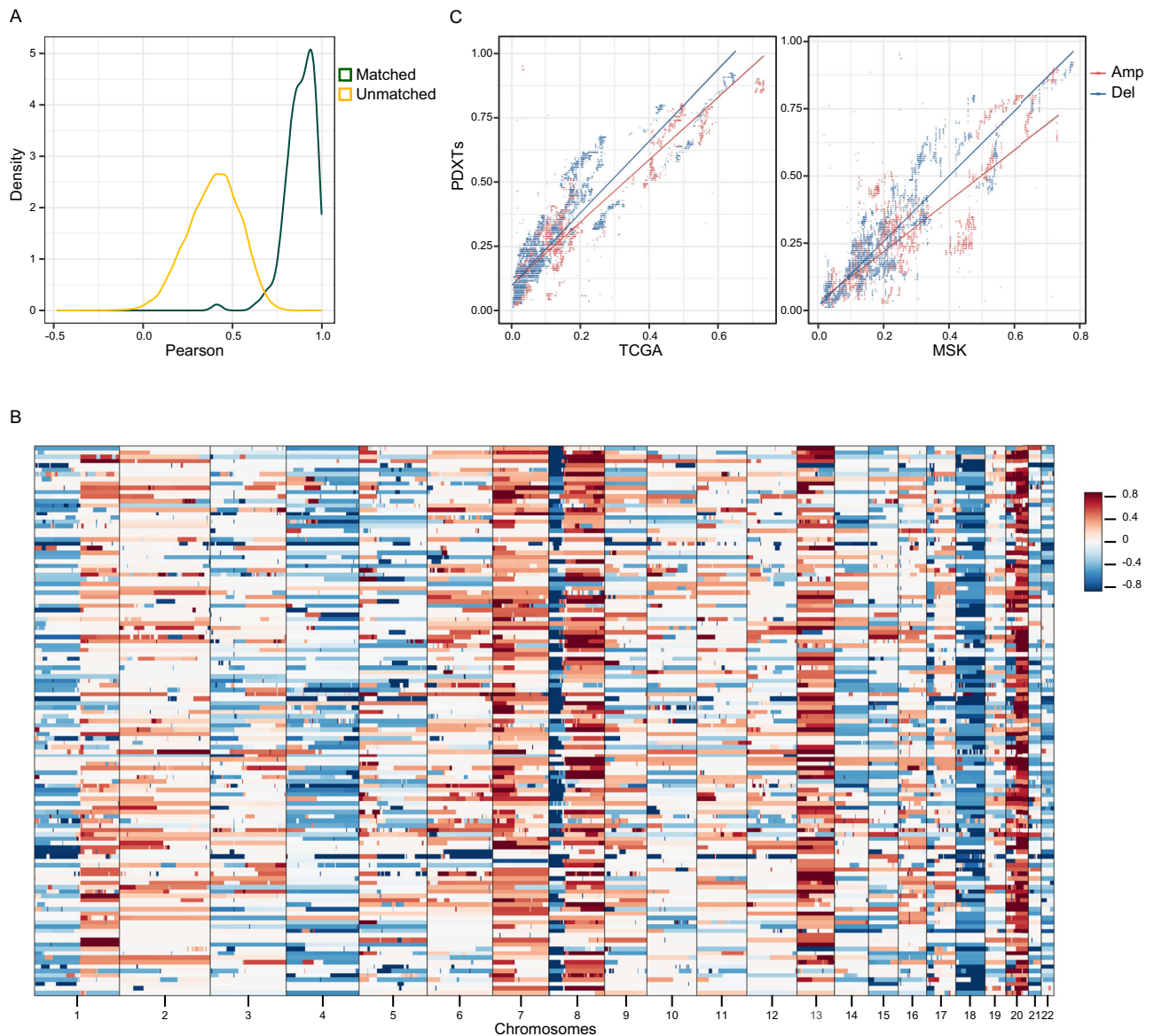


Fig. 3 | Comparative copy number architecture in paired PDXTs and PDXs.
A Distribution of Pearson correlation coefficients between copy number profiles of matched ($n = 125$) and unmatched ($n = 15,500$) pairs of PDXTs and PDXs.
B Autosomal copy number profiles of PDXTs ($n = 125$), expressed as segmented \log_2 ratio of the normalized read depth. Red and blue colors indicate gain and loss

events, respectively. **C** Gene-level population frequencies of gain or loss events, as identified by GISTIC, in PDXTs versus those detected in the TCGA or the MSK-IMPACT datasets. Amp amplification, Del deletion. Source data are provided as a Source Data file.

mutations in the *CTNNB1* gene (encoding β -catenin) were significantly over-represented in PDXTs that failed validation ($P = 0.002$, OR = 0.067, 95% CI 0.01–0.40) (Supplementary Fig. 7 and Supplementary Data 3). Both *CTNNB1* and *APC* mutations result in constitutive activation of the Wnt pathway, which sustains CRC proliferation. However, mutant β -catenin is known to be more modulatable by exogenous Wnt stimulation than mutant APC³¹. Since PDXTs were cultured in the absence of Wnt agonists, it is conceivable that *CTNNB1* mutant samples are less fit to grow in a nutrient-poor medium compared to *APC* mutant samples.

Most colorectal tumors display chromosomal instability, a condition that may be intensified by evolutionary bottlenecks such as those introduced during tissue culture propagation. To examine whether copy number changes materialized in our models following ex vivo culturing, we conducted low-pass whole genome sequencing in the same 125 PDX-PDXT pairs used for mutational profiling. This analysis revealed a high consistency in copy number variations between

PDXTs and the corresponding PDXs compared with unmatched samples (Pearson coefficient between segmented \log_2 ratios: median matched, 0.89, IQR 0.83–0.94; median unmatched, 0.40, IQR 0.30–0.50; $P = 1.92e-81$ by two-tailed Mann–Whitney test) (Fig. 3A). In PDXTs, the overall landscape of chromosomal alterations paralleled observations in patients²⁷. In particular, whole-arm copy number gains were detected in chromosomes 7, 13 and 20, and long-arm specific gains were detected in chromosome 1 and 8; whole-arm losses occurred in chromosome 18 (where the *SMAD4* gene lies) and in the short arms of chromosomes 1 and 8 (Fig. 3B). Accordingly, the population frequencies of copy number alterations (CNAs) at the gene level, obtained with GISTIC, showed positive correlations between PDXTs and the TCGA or MSK-IMPACT patient cohorts (Pearson coefficient, 0.92 [gains] and 0.87 [losses] for TCGA; 0.80 [gains] and 0.88 [losses] for MSK-IMPACT; $P < 1e-230$ by two-tailed Mann–Whitney test for both comparisons) (Fig. 3C). Similar correlations were observed between PDXs and the patient cohorts (Pearson coefficient, 0.92 [gains] and

0.90 [losses] for TCGA; 0.84 [gains] and 0.89 [losses] for MSK-IMPACT; $P < 1e-230$ by two-tailed Mann-Whitney test for both comparisons) (Supplementary Fig. 8). In summary, our data suggest that PDXTs generally retain the mutational and genomic structure of parental PDXs. Moreover, the distribution of major mutational drivers and CNAs observed in XENTURION PDXTs and PDXs is largely superimposable to that of human CRC samples.

PDX genomic patterns are largely preserved during PDXT serial passaging

To conduct a more precise investigation of potential genomic pattern alterations that may mark the transition from PDXs to PDXTs and to explore whether these patterns change with PDXT serial passaging, we generated whole exome sequencing data for a subset of 23 trios. These trios comprised donor PDXs, early-passage (third passage) PDXTs, and late-passage (passages from eight to 12) PDXTs from the same patient. Models were selected based on the representativeness in the distribution of high-frequency mutations (*APC* 14/23, 60.8%; *TP53* 16/23, 69.6%; *KRAS* 9/23, 39%) and the availability of quality-checked DNA in sufficient quantities for library preparation, including matched normal DNA as a reference for high-confidence annotation of somatic mutations and copy number variations. This deeper analysis in a more restricted subset of models confirmed the overall mutational and gene copy number concordance between paired PDXs and PDXTs observed in the larger cohort of 125 models, as previously evidenced through targeted sequencing and low-pass whole genome sequencing. The median Jaccard similarity coefficient for mutations with VAF > 0.05 was markedly higher for matched PDXs and early-passage PDXTs than for unmatched models (matched, 0.77, IQR 0.64–0.86; unmatched, 0.00, IQR 0.00–0.00; $P = 7.1e-39$ by two-tailed Mann-Whitney test) (Supplementary Fig. 9A). Likewise, the median Pearson correlation of copy number profiles was higher for matched models compared with unmatched samples (normalized depth ratio for matched samples, 0.94, IQR 0.91–0.95; unmatched, 0.55, IQR 0.46–0.62; $P = 4.831e-16$ by two-tailed Mann-Whitney test). We did not observe recurrent copy number gains or losses when comparing early PDXTs to matched donor PDXs (Supplementary Figs. 9B and 10A).

The substantial similarity in the mutational and copy number landscape exhibited by matched PDXs and early-passage PDXTs was maintained in late-passage models. High concordance was observed in early- and late-passage PDXT pairs when considering single-nucleotide alterations (median Jaccard index for matched pairs, 0.75, IQR 0.59–0.85; unmatched pairs, 0.00, IQR 0.00–0.00; $P = 7.6e-45$ by two-tailed Mann-Whitney test) (Fig. 4A) as well as gene copy number (median Pearson correlation between normalized depth ratios for matched samples, 0.93, IQR 0.88–0.95; unmatched, 0.56, IQR 0.50–0.62; $P = 4.887e-16$ by two-tailed Mann-Whitney test). No specific events of copy number gain or loss were detected in late- versus early-passage PDXTs (Fig. 4B and Supplementary Fig. 10B). These results are consistent with prior evidence showing that copy number profiles remain largely stable during PDX engraftment and serial passaging¹⁸.

We also examined potential loss of heterozygosity (LOH) events that may have occurred during PDXT derivation from PDXs or during tumoroid passaging by analyzing the frequency of minor alleles for heterozygous germline single-nucleotide polymorphisms (SNPs). When comparing parental PDXs to early-passage PDXTs, we did not observe any recurrent LOH gained during PDXT generation, only minor sporadic events (0.48% of the studied genomic regions). Conversely, there was a relatively high frequency of LOH events shared between donor PDXs and PDXTs (21.04%) (Supplementary Fig. 9C). Similarly, comparisons between early- and late-passage PDXTs revealed a low incidence of LOH events gained in late-passage models (0.19%) and a higher occurrence of shared LOH events (21.46%) (Fig. 4C). In both comparisons, we noted a small percentage of errors

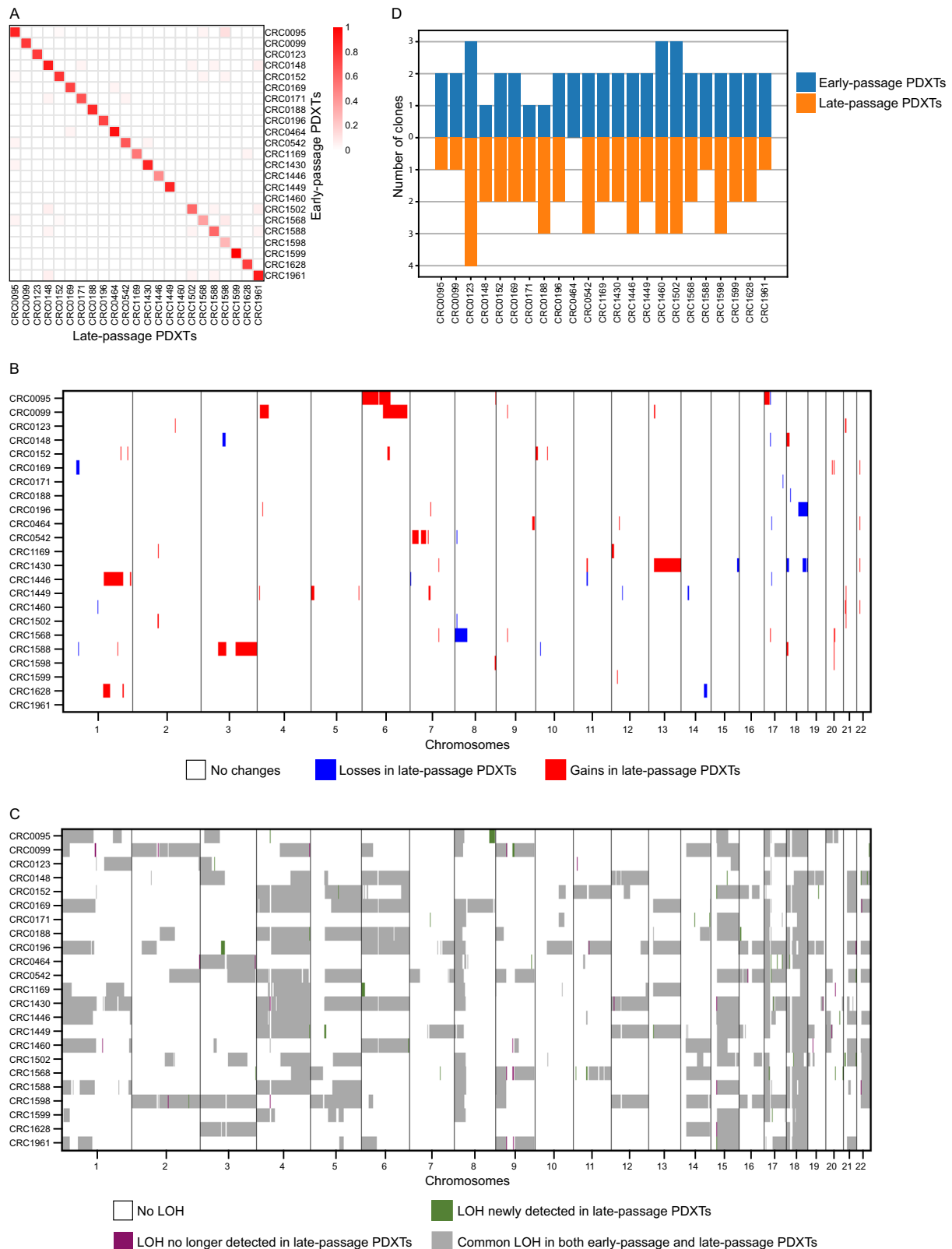
in LOH calls due to regions with a lost allele in PDXs not detected in early-passage PDXTs (0.16%), or regions with a lost allele in early-passage PDXTs not detected in the late-passage counterparts (0.07%). These infrequent errors are likely attributable to intrinsic noise in the segmentation and calling procedure.

Finally, we explored tumor heterogeneity across matched models from the same patient by estimating variations in the number of subclones using PyClone-vi. This tool infers the number of clones from single-nucleotide variants, small indels and CNAs, and produces an output that includes the probability of assignment of a mutation to a specific subclone (thereby identifying a subclone as a cluster of mutations) and the number of mutations belonging to a cluster³². By applying filters with a 50% probability threshold and a minimum of 10 mutations for cluster definition, we found that all models were oligoclonal, with most consisting of 2–3 clusters. Discernible yet modest variations in clonal architecture were observed in approximately 50% of the analyzed trios. Among PDXs and early-passage tumoroids, 13 models maintained the same number of clusters, while five early-passage tumoroids gained one cluster and five lost one cluster compared with originating PDXs (Supplementary Fig. 9D). In comparisons of late- versus early-passage PDXTs, 11 models exhibited the same clonal organization, seven late-passage PDXTs gained one or two clusters, and five lost one or two clusters (Fig. 4D). These findings suggest no overt differences in subclonal heterogeneity between PDXs and PDXTs, as well as between early- and late-passage PDXTs. Overall, the various levels of genomic analysis in parental PDXs, early-passage PDXTs, and late-passage PDXTs did not reveal substantial drifts caused by the experimental workflow, while providing a more detailed landscape of the molecular features characterizing XENTURION models throughout their lifespan.

PDXT transcriptional identity retains fidelity to corresponding PDXs and is stable over time

Transcriptomic data were used to compare the gene expression profiles of 21 surgical specimens from donor patients (human liver metastases, HLMs), 119 PDXs from which PDXTs were successfully derived and validated, and 124 validated PDXTs, all chosen for meeting standard RNA quality criteria for sequencing. Based on gene ontology (GO) enrichment analysis of differentially expressed genes, gene signatures related to cellular division and DNA replication were more abundant in PDXs than HLMs, consistent with the faster growth rates of xenografts compared with those of tumors in patients³³ (Supplementary Data 4). Pathways downregulated in PDXs versus HLMs were associated with innate and adaptive immunity and stromal remodeling (Supplementary Data 4), as expected for models grown in immunocompromised animals and in agreement with the observation that human stromal cells are replaced by mouse components soon after tumor implantation^{34,35}. Being derived from PDXs, PDXTs predictably showed similar upregulated and downregulated pathways with respect to HLMs (Supplementary Data 4).

Comparative analysis of xenografts and validated tumoroids revealed that gene signatures of steroid, retinoid and fatty acid metabolism were more expressed in PDXTs than in PDXs (Supplementary Fig. 11 and Supplementary Data 4). This may be attributed to metabolic adaptations to the culture conditions and is in line with previous results obtained in a smaller set of 19 CRC PDX/tumoroid sibling pairs³⁶. A cluster of gene sets functionally related to cellular response to innate immunity pathways stood out as significantly downregulated in PDXTs compared to PDXs (Supplementary Fig. 11 and Supplementary Data 4), likely as a result of the depletion of host innate immune cells during the transition from in vivo tumors to ex vivo cultures. Additionally, to gain deeper insights into the molecular characteristics that may impact tumoroid establishment, we analyzed differentially expressed genes between the 119 PDX samples with accompanying RNAseq data that had successfully produced



validated PDXTs and 49 PDX samples from which tumoroid early derivation or validation had failed. This analysis identified 328 downregulated genes and 113 upregulated genes in PDXs that successfully originated tumoroids compared to unproductive PDXs. GO annotation of the downregulated genes indicated an enrichment for signatures associated with epithelial squamous differentiation ('keratinocyte differentiation' GO term, adjusted $P=1.17e-6$ by one-tailed Fisher's exact

test), whereas upregulated genes exhibited features related to extracellular matrix components ('collagen-containing extracellular matrix' GO term, adjusted $P=3.76e-2$ by one-tailed Fisher's exact test) (Supplementary Fig. 12A and Supplementary Data 4). This suggests that PDX models with low expression of epithelial differentiation markers and high expression of extracellular matrix molecules are more likely to establish tumoroids.

Fig. 4 | Comparative genomic landscape in matched early- and late-passage PDXTs. **A** Jaccard similarity indexes of somatic alterations (VAFs > 0.05) between 23 matched early- and late-passage PDXTs. The Jaccard index for model CRC1460 is 0, likely due to low tumor mutational burden (TMB) (1.96 mutations [mut] per mega base pairs [Mbps] in early-passage PDXTs and 2.13 muts/Mbps in late-passage counterparts; median TMB for all-early passage PDXTs, 5.4 muts/Mbps, IQR 4.5–6.1; median TMB for all late-passage PDXTs, 5.7 muts/Mbps, IQR 4.8–6.7). CRC1460 low TMB, coupled with variant annotation limited to PCGR tiers ≤ 3 (enriched for mutations with stronger potential relevance for cancer, see “Methods” section), resulted in detecting only a single alteration exclusively in the late-passage PDXT. **B** Comparison of autosomal copy number profiles between 23 matched early- and late-passage PDXTs. ‘No changes’ refers to stable or quasi-stable regions. ‘Losses in late-passage PDXTs’ are defined as loci with copy number ≤ 1 in the late-passage PDXTs and ≥ 2 in the early-passage counterparts. ‘Gains in late-passage PDXTs’ are defined as loci with copy number ≥ 5 in the late-passage PDXTs

but not in the early-passage counterparts. The genome is represented by 100k base pair long bins; each row in the heatmap represents a pair of matched early- and late-passage PDXTs. **C** Comparison of LOH events between 23 matched early- and late-passage PDXTs. ‘No LOH’ indicates regions without LOH in both early- and late-passage pairs. ‘LOH newly detected in late-passage PDXTs’ indicates regions with newly acquired LOH events in the late-passage PDXTs that are not present in the early-passage counterparts. ‘LOH no longer detected in late-passage PDXTs’ indicates regions with LOH events detected in the early-passage PDXTs that are no longer detected in the late-passage counterparts. ‘Common LOH in both early- and late-passage PDXTs’ indicates regions with LOH events shared between sibling pairs. The genome is represented by 100k base pair long bins; each row in the heatmap represents a pair of matched early- and late-passage PDXTs. **D** Number of clusters (clones) inferred by PyClone-vi in 23 matched early- and late-passage PDXTs. Source data are provided as a Source Data file.

To investigate the transcriptional fidelity of PDXT-PDX pairs, we first considered a subset of 79 ‘super-matched’ samples selected based on genealogical proximity (i.e., pairs made of an early-passage PDXT with its nearest ancestor PDX). This analysis showed high consistency in transcript abundance between samples, with an intramodel Pearson correlation coefficient significantly greater than intermodel correlations (median matched, 0.83, IQR 0.80–0.85; median unmatched, 0.62, IQR 0.57–0.66; $P = 3.477e-52$ by two-tailed Mann–Whitney test) (Fig. 5A). We then extended the survey to a more variegated set of sample families, which included early and late propagations from the same PDXT and one or more matched PDXs grown in more distant generations of mice. In this larger set, consisting of 116 PDX/PDXT sibling models for a total of 308 data points (including replicates), the similarity between matched PDXTs and PDXs was confirmed; in particular, the intramodel Pearson correlation coefficient was significantly higher than intermodel correlations (median matched, 0.78, IQR 0.75–0.81; median unmatched, 0.52, IQR 0.50–0.54; $P = 1.50e-39$ by two-tailed Mann–Whitney test), and 80/116 (69%) models derived from the same originating tumor proved to belong to the same cluster by unsupervised hierarchical clustering (Supplementary Fig. 12B). We noted that the transcriptional profile of tumor CRC1241, which had a very high PDXT-PDX correlation (Pearson coefficient, 0.90), was different from the rest of our cohort (average Pearson coefficient, 0.31) (Fig. 5A). Accordingly, a deep-learning tool that uses RNA gene expression data to infer a tumor’s primary tissue of origin³⁷ predicted the tumor as a cervical squamous cell carcinoma (Supplementary Data 5), and post hoc pathological revision cataloged it as an anal squamous cell carcinoma. For this reason, we excluded CRC1241 from further analyses.

To explore whether tumoroid propagation leads to any transcriptional drift, we examined differentially expressed genes between the early- and late-passage PDXTs that were also utilized for the genomic comparisons. Only 30 genes were significantly downregulated in late-passage tumoroids compared to their early-passage counterparts, with no genes found to be upregulated. This finding indicates a substantial conservation of transcriptomic profiles across serial passaging. This consistency was further corroborated by correlation analyses (median Pearson coefficient, 0.920; IQR for matched models, 0.86–0.94; IQR for unmatched models, 0.39–0.52) (Fig. 5B).

Gene expression profiling has been recently deployed to develop CRC classifiers with prognostic and predictive significance. The Consensus Molecular Subtypes (CMS) classifier was built on whole-tumor transcriptomes (including cancer cell and stromal/immune transcripts)³⁸, whereas the CRC Intrinsic Signature (CRIS) classifier utilized PDX gene expression datasets to derive cancer cell-specific subtypes³⁵. We first assigned each PDXT and PDX of the ‘super-matched’ 79 pairs to a CMS or CRIS subtype. Plausibly, many models failed CMS categorization due to lack of human stroma, which greatly contributes to CMS subtype assignment^{34,35,39}. Conversely, all models

received a CRIS designation (Fig. 5C). We then evaluated the consistency in subtype assignment using a tailored version of the Jaccard index, whereby the number of models with the same subtype in matched PDXs and PDXTs was divided by the total number of models assigned to that subtype. This index revealed good overall correspondence, with average values across subtypes of 0.44 for both CMS and CRIS. At the level of individual subtypes, a general stability in class assignment was observed with the exception of CMS4 (Fig. 5C). Specifically, the consistency index between PDXs and PDXTs was 0.69 for CMS1; 0.48 for CMS2; 0.40 for CMS3; 0.18 for CMS4; 0.45 for samples that failed CMS classification; 0.43 for CRIS-A; 0.33 for CRIS-B; 0.55 for CRIS-C; 0.41 for CRIS-D; and 0.45 for CRIS-E. The poor performance of PDX and PDXT class assignment to CMS4 is expected, as CMS4 characteristics are dominantly driven by human stromal transcripts that are absent in XENTURION models. PDXTs therefore display representative gene expression profiles that define their identity with parental PDXs and allow their classification into RNA expression-based CRC subtypes without a substantial culture bias.

PDXT sensitivity to cetuximab is concordant with PDX response in a large-scale population trial

The anti-EGFR antibody cetuximab is a standard-of-care treatment with demonstrated clinical benefit in patients with inoperable RAS/RAF wild-type metastatic CRC⁴⁰. We and others have used PDX-based resources to identify determinants of responsiveness and resistance to cetuximab and to nominate novel druggable targets for cetuximab-resistant tumors^{14–17,36,41}. As a consequence, a large part of XENTURION’s PDXTs were derived from PDX models for which annotation of sensitivity to cetuximab was available. We leveraged this information to investigate how and to what extent PDXTs may act as functional ex vivo surrogates of therapeutic profiles in xenografts.

Sensitivity to cetuximab was assessed in 119 validated PDXTs with growth characteristics and manipulability suitable for pharmacologic experiments. Each model was plated at three different cell densities (1250, 5000 and 20,000 cells/well) in a 96-well format and cultured for one week in the presence or absence of 20 $\mu\text{g/ml}$ cetuximab without EGF (which competes with the antibody for receptor binding). The selected antibody concentration was based on existing literature data and represented an intermediate dose reported to achieve an inhibitory plateau across CRC cell lines and tumoroids^{9,17,36,42,43}. The response was determined by measuring the ratio between treated and untreated cells and using as readouts endpoint luminescent ATP content and longitudinal cell imaging, for a total of 6174 measurements. A coefficient of variation (CV) was calculated to evaluate consistency between biological triplicates. Based on these CV measurements, 116 PDXT models with above-threshold inter-experiment consistency (see Methods) were selected for further analyses.

The experimental setting was overall robust and reproducible, as documented by the significant correlations between luminescence-

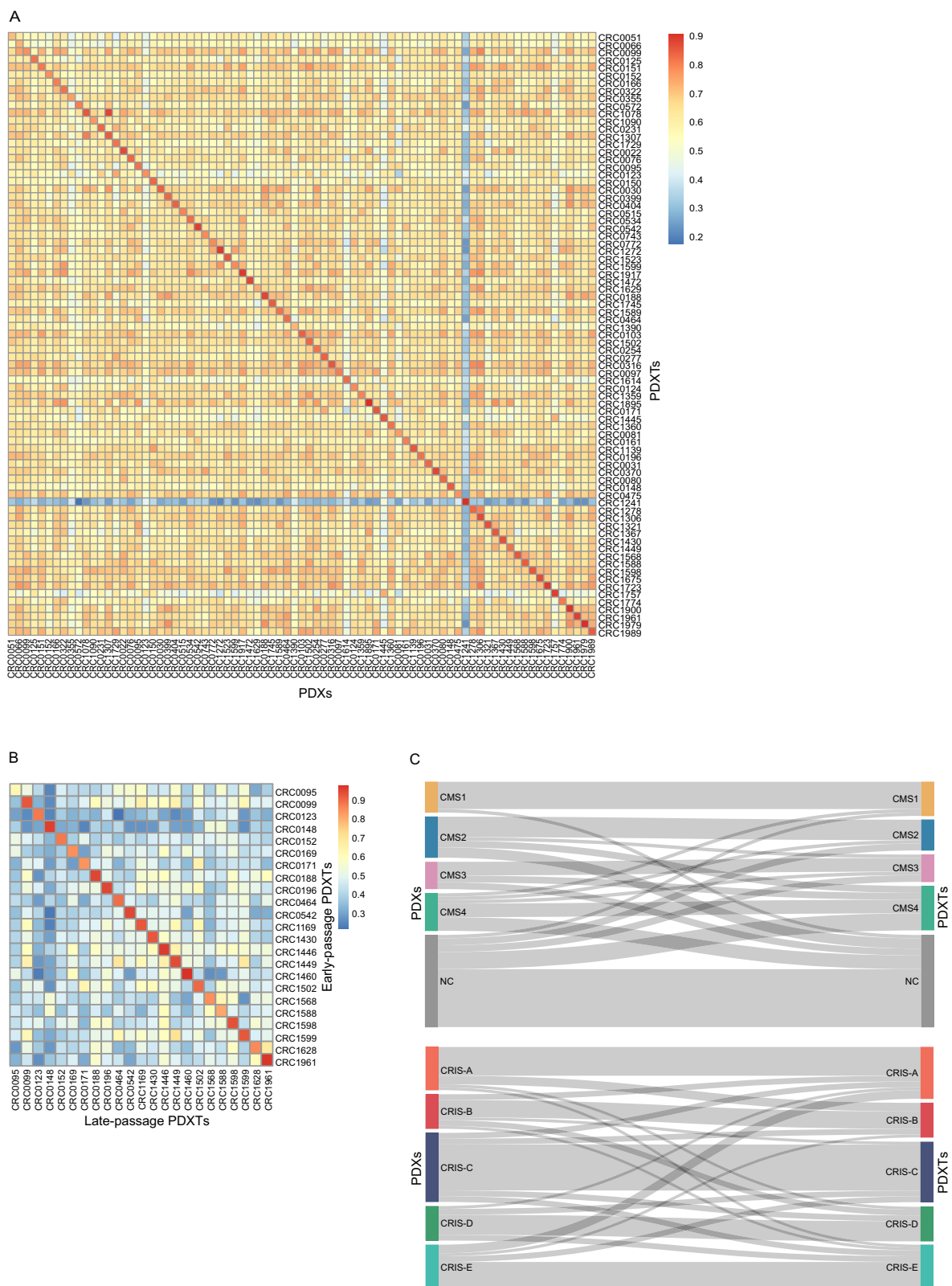


Fig. 5 | Comparative gene expression profiles and transcriptional subtype assignment in paired PDXTs and PDXs. A Pearson correlations of gene expression profiles in matched PDXs and PDXTs. Pearson correlation coefficients were calculated for matched ($n = 79$) and unmatched ($n = 6,162$) pairs. **B** Pearson correlations

of gene expression profiles in matched early- and late-passage PDXTs. Pearson correlation coefficients were calculated for matched ($n = 23$) and unmatched ($n = 506$) pairs. **C** CMS and CRIS subtype assignment in 79 pairs of matched PDXTs and PDXs. NC non-classified. Source data are provided as a Source Data file.

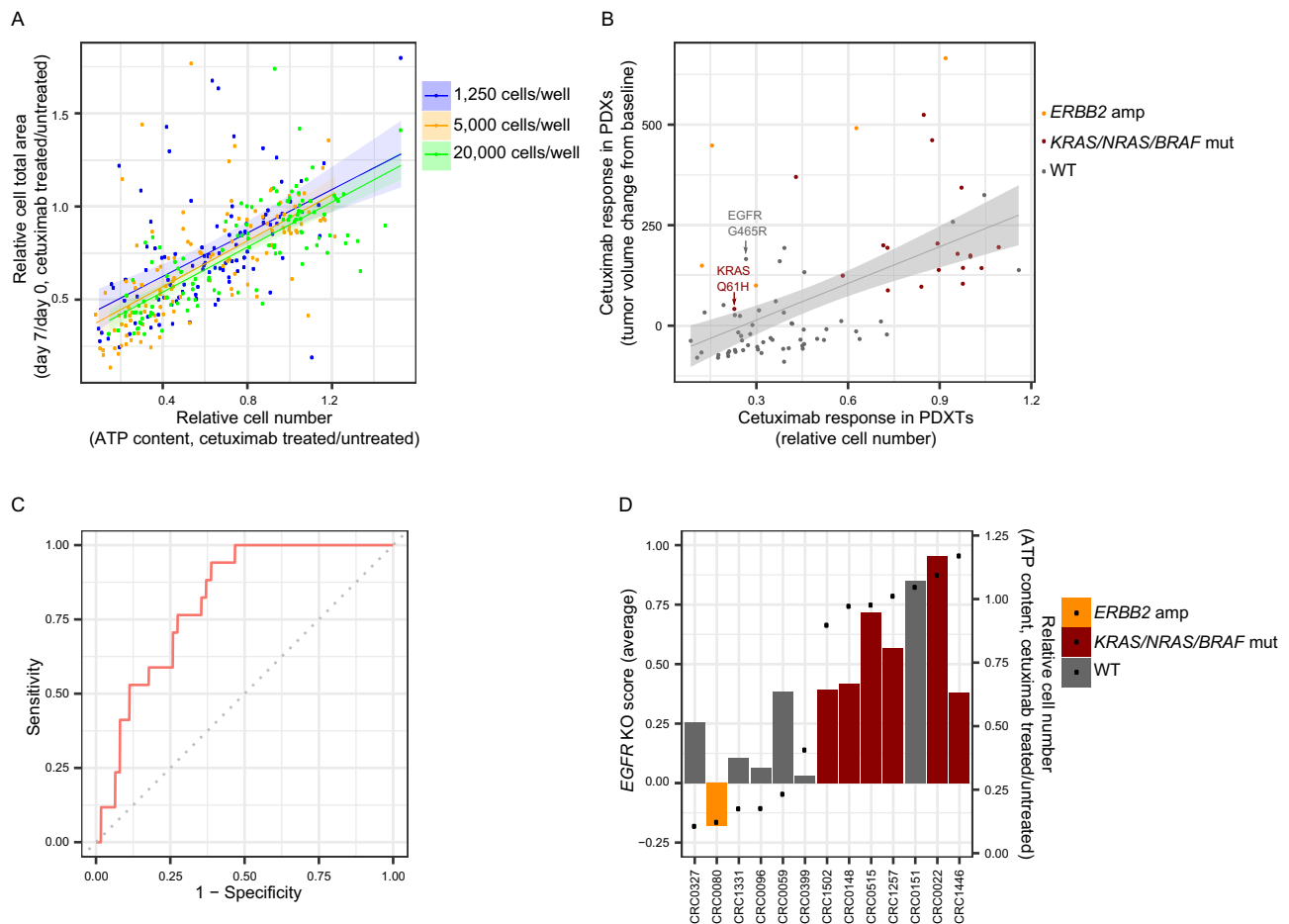


Fig. 6 | Comparative annotation of cetuximab response profiles in paired PDXTs and PDXs. A Correlation of cetuximab response between values of end-point ATP content (relative cell number) and values obtained by longitudinal cell imaging (relative tumoroid total area) in 116 PDXTs plated at different cell densities and treated with cetuximab (20 $\mu\text{g}/\text{ml}$) for one week. Each dot represents one single experiment performed in biological triplicate. Responses were assessed in 116 models for 5000 and 20,000 cells/well, and 102 models for 1250 cells/well. The shaded area represents the confidence interval of linear model prediction, 95%. **B** Correlation of cetuximab response in 79 pairs of matched PDXTs and PDXs. Response in PDXTs was evaluated as the ratio of viable cells after one week of treatment (20 $\mu\text{g}/\text{ml}$ cetuximab, 5000 cells/well in a 96-well format) to untreated controls; response in matched PDXs implanted in both male and female NOD-SCID

mice was evaluated as the percentage of tumor volume variation after three weeks of treatment (20 mg/kg, intraperitoneal injection twice a week) compared with tumor volume the day before treatment initiation. The shaded area represents the confidence interval of linear model prediction, 95%. **C** ROC curve showing the performance of PDXT-based results in predicting cetuximab response in vivo in 79 pairs. AUC, 0.81; responders (target prediction), 17; non-responders, 62. **D** *EGFR* KO scores for 13 PDXTs, distributed according to cetuximab sensitivity (black dots). Results are the average of the mean effect size of two sgRNAs against *EGFR* in two independent experiments, each performed in biological triplicates (with the exception of CRC0148, which was tested in three independent experiments). KO knockout, WT wild-type, amp amplification, mut mutation. Source data are provided as a Source Data file.

based and imaging-based detection for all cell plating densities (Pearson coefficient, 0.52; $P = 1.7\text{e-}8$ [1250 cells]; 0.65; $P = 1.4\text{e-}15$ [5000 cells]; 0.77; $P = 5.5\text{e-}24$ [20,000 cells]), and resulted in a graded distribution of responsiveness to cetuximab treatment (Fig. 6A). We then used linear regression models to compare all these PDXT measurements with the in vivo tumor response (defined as the relative volume change after three weeks of treatment) in 79 matched PDXs for which cetuximab therapeutic annotation was available (Supplementary Data 6). Also in this case, correlations were all positive and significant, with ATP values for the 5000 cell-plating density showing the best performance (Pearson coefficient, 0.56, $P = 9.9\text{e-}8$) (Fig. 6B and Supplementary Fig. 13A). Additionally, a significant, albeit slightly lower, concordance in cetuximab response between PDXs and PDXTs was observed when in vivo therapeutic sensitivity was measured by calculating tumor growth inhibition (TGI) scores, which compare tumor growth in the cetuximab-treated group to tumor growth in mice exposed to placebo (Pearson coefficient, 0.47; $P = 5.5\text{e-}4$) (Supplementary Fig. 13B and Supplementary Data 6). For this analysis, data were available for only 51 PDXs because some mice in the placebo arms

had to be euthanized before the end of the three-week monitoring period due to reaching the humane endpoint. We attribute the reduced statistical significance observed with this alternative metric to the smaller sample size of the PDX-PDXT pairs included in the analysis.

Next, we analyzed cetuximab response in relation to genetic biomarkers known to confer resistance to cetuximab in patients. In line with clinical observations, tumors harboring *KRAS*, *NRAS* or *BRAF* mutations were generally refractory to EGFR blockade in both platforms (15 models out of 18 had a luminescence ratio > 0.7 when tested as PDXTs and a growth increase of more than 70% when tested as PDXs) (Fig. 6B). However, we also found some discrepant examples. First, one *KRAS* Q61H mutant model that had been categorized as a mild non-responder in vivo (relative tumor volume increase after three weeks of treatment, 42.35%) proved to be sensitive in the corresponding PDXTs (treated/untreated luminescence ratio, 0.23) (Fig. 6B). Interestingly, heterogeneous responses of *KRAS* Q61H mutant metastatic CRC tumors to anti-EGFR antibodies have also been observed in patients^{44,45}. Second, a model with a subclonal cetuximab resistance mutation in the originating tumor (*EGFR* G465R, VAF 0.195)

showed overt resistance in PDXs (relative tumor volume increase after three weeks of treatment, 166.5%) but appreciable sensitivity in the matched PDXT (treated/untreated luminescence ratio <0.3) (Fig. 6B). In this case, the disconnect between PDX and PDXT data is due to sampling bias; the PDXs used for monitoring tumor response to cetuximab *in vivo* harbored the *EGFR* G465R mutation, whereas the PDXTs used for the *ex vivo* drug screen were derived from a sibling xenograft where the alteration was absent. The final element of divergence was found for *ERBB2* amplification, which predicts poor response to EGFR inhibition in patients with metastatic CRC^{46,47}. As shown previously^{14,16}, *ERBB2*-amplified PDXs failed to respond to cetuximab (Fig. 6B); however, this resistant phenotype was only partially recapitulated in PDXTs, with three models out of five displaying a certain degree of sensitivity (treated/untreated luminescence ratio ≤ 0.3) (Fig. 6B). The signaling and transformation potency of HER2 in *ERBB2*-amplified tumors is tunable by EGF stimulation⁴⁸. On this ground, we speculate that the HER2 bypass pathway that blunts response to EGFR inhibition was below threshold in some PDXTs due to lack of EGF in the culture medium (thus, tumoroids retained sensitivity to cetuximab); conversely, the widespread availability of murine EGF in PDXs stimulated HER2 signaling to an extent sufficient to impart resistance to EGFR inhibition *in vivo*.

We reasoned that results from this population trial might prove valuable to formalize the predictive accuracy of PDXTs in modeling PDX experiments. The overall area under the curve to distinguish overtly responsive PDXs (relative tumor volume shrinkage after three weeks of treatment $> 50\%$) from those that remained stable or progressed while on treatment was 0.81 (Fig. 6C). Based on this ROC analysis, a luminescence ratio of 0.4 in PDXTs identified 94% of matched PDXs that responded to treatment with tumor regression (Supplementary Data 6). However, the positive predictive value of pharmacologic assays in PDXTs was relatively low (FDR = 0.6), confirming the importance of model-matched *in vivo* validation during the preclinical phases of drug development. These considerations illustrate the merit of assessing the efficacy of a specific drug in a vast collection of tumoroids to advise the rational selection of models for PDX experiments.

Gene editing recapitulates the outcome of pharmacologic target inhibition in PDXTs

Cancer dependency maps, obtained by perturbing genes with RNA interference or gene editing technologies, have provided a catalog of tumor vulnerabilities with potential clinical actionability^{49,50}. These efforts have been traditionally pursued in immortalized cancer cell lines, but there is now increasing recognition that functional genomics screens in tumoroids would be better representative of cancer biology and diversity⁵¹. With this in mind, we sought to explore whether genetic versus pharmacologic inhibition of an index cancer dependency gene results in similar or different effects on PDXT viability. Given the large number of models with known response to cetuximab, EGFR was selected as a target, and CRISPR-Cas9 technology was employed to systematically disrupt the *EGFR* gene in 13 representative PDXTs with variable sensitivity to cetuximab and proven amenability to lentiviral transduction.

Two different sgRNAs targeting *EGFR* in exon three were independently transduced into Cas9-expressing PDXTs (Supplementary Figs. 14 and 15A, B). Seven days after infection, tumoroids were processed for luminescence-based detection of ATP content. A knockout (KO) score was calculated by intra-model normalization of the viability outputs of *EGFR*-edited PDXTs to conditions of negligible influence on cell fitness (deletion of a neutral/non-essential gene) or strong influence (deletion of a lethal/essential gene) (see “Methods” section). The consequences of *EGFR* deletion on PDXT viability were similar for the two sgRNAs (Pearson coefficient, 0.84, $P = 3.3e-4$) (Supplementary Fig. 15C), supporting robustness and reproducibility of the dataset.

Remarkably, the overall outcome of *EGFR* genetic ablation was significantly correlated to that of cetuximab treatment (Pearson coefficient, 0.78, $P = 0.0016$), and in some cases a direct quantitative correspondence between the extent of pharmacologic sensitivity and the impact of gene deletion could be observed (Fig. 6D); for example, a RAS wild-type model that proved to be highly refractory to cetuximab treatment was also poorly impacted by *EGFR* disruption (CRC0151); in a complementary fashion, *EGFR* KO was severely detrimental in an *ERBB2*-amplified PDXT that was also particularly sensitive to cetuximab (CRC0080) (Fig. 6D). Collectively, these findings underscore the power and reliability of using genetic approaches in tumoroids for preclinical characterization of drug targets and to interrogate the effects of loss-of-function alterations in cancer-relevant genes.

An *in silico*, *ex vivo* and *in vivo* funneling approach identifies actionable co-dependencies that attenuate response to cetuximab

The concordance of molecular profiles and therapeutic annotation in matched PDXTs and PDXs prompted us to embark on a discovery effort aimed to identify adaptive dependencies in models that were sensitive to, but not eradicated by, EGFR inhibition. To do so, we followed a principled approach meant to triage candidate vulnerabilities using sequential selection bottlenecks, with the final aim to nominate only those targets that passed strict validation criteria.

We started by analyzing transcriptional responses to drug pressure in cetuximab-sensitive models (33 PDXs and 12 PDXTs) treated with the antibody, with the assumption that some upregulated gene products may adaptively convey compensatory signals to contrast EGFR inhibition. Similar to basal (pre-treatment) profiles, also on-treatment gene expression changes were coherent in PDXTs and PDXs (Pearson coefficient, 0.8; $P < 2.2e-308$) (Fig. 7A). The list of genes that were upregulated by cetuximab in all PDXs and PDXTs examined was refined by removing low-expressed ones and those that were also modulated by treatment in an independent set of 21 cetuximab-resistant PDXs. The resulting compendium of 1916 genes was restricted to a subset of 119 genes encoding druggable targets, based on a two-tiered selection strategy: (i) a target tractability assessment using published criteria⁵⁰, such as the availability of compounds in clinical or preclinical development and/or the documentation of an associated response biomarker; (ii) data output from the Drug-Gene Interaction Database (www.dgidb.org), a web resource that provides information on drug-gene interactions and druggable genes. The 119 gene subset was further narrowed down to 13 candidates through a shortlisting process that considered target conceptual novelty and translational potential as well as known potency and *in vivo* bioavailability of the corresponding specific drugs (Supplementary Fig. 16 and Supplementary Data 7).

To preliminarily assess whether the prioritized hits were valuable therapeutic targets, we performed short-term (48 h) viability assays using well-characterized chemical inhibitors of the 13 candidates. Each inhibitor was tested in three PDXTs in the absence or presence of cetuximab, with model selection guided by robust cetuximab-induced overexpression of the targeted gene (in most cases, one or more models were used to test more than one drug) (Supplementary Data 8). The compounds were evaluated in a four-point dose-response assay with biological triplicates and in three independent experiments, using the conditions that proved to be the most accurate in recapitulating response *in vivo* (5000 cells/well in a 96-well format and luminescence-based detection of ATP content as viability readout), for a total of 3510 measurements (Supplementary Fig. 17). Drug doses were calibrated using literature data and publicly available pharmacologic profiles⁵², with a maximum dose for each inhibitor equal to twice the standard IC_{50} value. From this first set of assays, three compounds stood out for having the highest maximum inhibition score as single agents (i.e., their maximum dose had the strongest

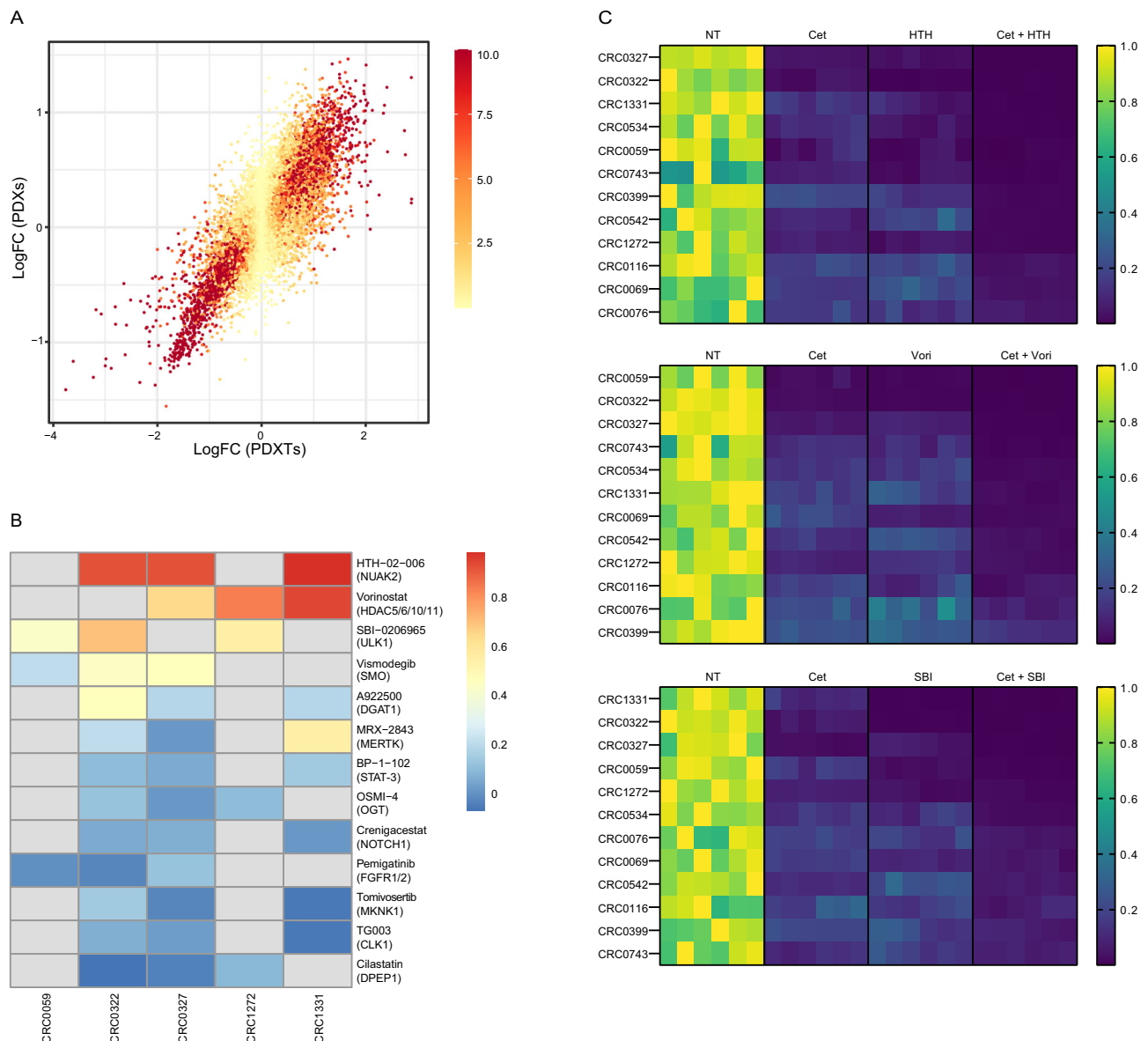


Fig. 7 | Drug screen in PDXTs. A Correlation of transcript changes between 33 PDXs exposed to cetuximab for three days ($n = 28$) or six weeks ($n = 6$) and 12 PDXTs exposed to cetuximab for three days. The scatterplot shows log-fold changes (LogFC) between treated and untreated samples for 19,716 genes. Color shading reflects differential expression P values, obtained with DESeq2. Statistical analysis by two-sided Wald test followed by Benjamini-Hochberg multiple comparison correction. **B** Maximum inhibition scores for 13 drugs tested in three PDXTs. PDXTs were treated for 48 h (5000 cells/well) in three independent experiments in biological triplicates. Maximum inhibition score was the difference between the viability of untreated cells and that at maximum drug dosage, normalized against the viability of untreated cells and averaged for results of the three independent experiments. Maximum drug dosage: HTH-02-006, 16 μM ; vorinostat, 10 μM ; SBI-0206965, 20 μM ; vismodegib, 50 μM ; A922500, 100 μM ; MRX-2483, 1 μM ; BP-1-102, 1 μM ; OSMI-4, 20 μM ; crenigacestat, 5 μM ; pemigatinib, 1 μM ; tomivosertib, 5 μM ; TG003, 50 μM ; cilastatin, 0.5 μM . Drug targets are specified.

C Cell viability in 12 PDXTs treated for 3 weeks (CRC0059 and CRC0322, 1000 cells/well) or 1 week (all other models) with SBI-0206965 (10 μM), HTH-02-006 (4 μM), and vorinostat (1.25 μM), alone or with cetuximab (20 $\mu\text{g}/\text{ml}$, one-week treatments; 5 $\mu\text{g}/\text{ml}$, three-week treatments). Two independent experiments in biological triplicates were performed. Heatmap signals were normalized to the sum of the values of the corresponding experiments and reported as a fraction of the maximum value reached by single models. Statistical analysis by repeated measures one-way ANOVA followed by Šidák's multiple comparison test using the aggregated average value of replicates for each PDXT model ($n = 12$): cetuximab versus cetuximab + SBI-0206965, $P < 0.0001$; SBI-0206965 versus cetuximab + SBI-0206965, $P = 0.0021$; cetuximab versus cetuximab + HTH-02-006, $P < 0.0001$; HTH-02-006 versus cetuximab + HTH-02-006, $P = 0.0027$; cetuximab versus cetuximab + vorinostat, $P < 0.0001$; vorinostat versus cetuximab + vorinostat, $P = 0.0006$. Cet cetuximab, HTH HTH-02-006, SBI SBI-0206965, Vori vorinostat. Source data are provided as a Source Data file.

impact on cell viability) (Fig. 7B and Supplementary Data 9): HTH-02-006, targeting NUA2, a member of the AMPK subfamily of serine/threonine protein kinases; vorinostat, targeting histone deacetylases (HDACs); and SBI-0206965, targeting the serine/threonine kinase ULK1. Interestingly, these targets are variably involved in promoting autophagy, a homeostatic mechanism triggered by cellular stress⁵³.

Blockade of the 13 candidate targets in combination with cetuximab incrementally reduced cell viability, again with HTH-02-006, vorinostat and SBI-0206965 showing the highest maximum inhibition scores (Supplementary Fig. 17 and Supplementary Data 9). We then explored the interaction between cetuximab and these three top inhibitors under conditions of longer drug exposure to favor the

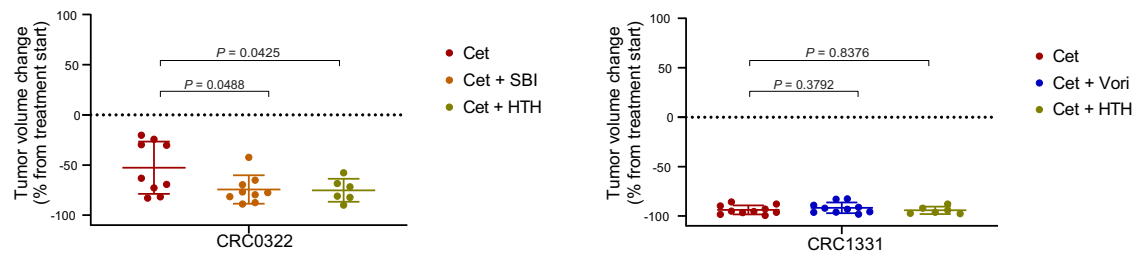


Fig. 8 | Drug screen validation in representative PDXs. Tumor volume changes in PDXs implanted in female NOD-SCID mice and exposed to the indicated modalities for 4 weeks. Cetuximab, 20 mg/kg (intraperitoneal injection twice a week); HTH-02-006, 10 mg/kg (intraperitoneal injection twice a day); SBI-0206965, 20 mg/kg (intraperitoneal injection three times a week); vorinostat, 50 mg/kg (intraperitoneal injection three times a week). Dots represent volume changes of PDXs from individual mice, and plots show the means \pm SD for each treatment arm. $n = 6$ for

CRC0322 and CRC1331 models exposed to HTH-02-006 + cetuximab; $n = 9$ for CRC0322 model exposed to cetuximab or SBI-0206965 + cetuximab; $n = 10$ for CRC1331 model exposed to cetuximab or vorinostat + cetuximab. Tumor volume changes of the placebo arm are shown in Supplementary Fig. 18. Statistical analysis by two-tailed unpaired t test with Welch's correction. Cet cetuximab, HTH HTH-02-006, SBI SBI-0206965, Vori vorinostat. Source data are provided as a Source Data file.

implementation of adaptive reactions over time. This analysis was extended to the full set of 12 cetuximab-sensitive PDXTs with available gene expression data. In all tested models, combination therapy with cetuximab and either HTH-02-006, vorinostat or SBI-0206965 was significantly more effective than single-agent treatments and outperformed cetuximab monotherapy (Fig. 7C).

Finally, pharmacologic experiments were translated into the in vivo setting. PDX model CRC0322 was chosen for administration of HTH-02-006 and SBI-0206965 because the corresponding PDXT was particularly sensitive to both drugs; following a similar reasoning, PDX model CRC1331 was chosen because the matched PDXT displayed the highest maximum inhibition score for both vorinostat and HTH-02-006 (Fig. 7B). As expected, both PDX models were strong responders to cetuximab monotherapy (Fig. 8). While single agent-treatment with HTH-02-006, vorinostat or SBI-0206965 had negligible or null effect on tumor growth (Supplementary Fig. 18), the combination of HTH-02-006 or SBI-0206965 with cetuximab proved to be more effective than cetuximab alone in reducing tumor size in CRC0322 PDXs (Fig. 8). In CRC1331, combination therapy of cetuximab with either vorinostat or HTH-02-006 did not significantly outperform cetuximab monotherapy (Fig. 8); however, it is worth noting that response to cetuximab was exceptionally profound in this PDX (mean tumor volume decrease, 93.77%), which may have masked the contribution of the other drug to tumor regression. In essence, these results emphasize the value of integrative molecular and biological data, coupled with vast availability of experimental models, for 'aggressive' prioritization of targets with meaningful translational potential.

Discussion

Several cancer centers have shared their PDX models in distributed repositories to achieve a comprehensive representation of study populations. These consortial initiatives, such as PDXNet and EuroPDX, aim to establish ample PDX platforms for use by the global scientific community and to develop consensus guidelines for standard operating procedures and metadata harmonization^{18,54–56}. Despite these advances, public collections that include matched PDXs and tumoroids with accompanying molecular, pharmacologic and methological annotations remain scarce.

XENTURION is a living biobank of matched xenografts and tumoroids from patients with metastatic CRC, with associated multi-dimensional molecular data and biological annotation. A similar resource has been recently developed for treatment-refractory and metastatic breast cancers⁵⁷. Models in XENTURION recapitulated the genetic heterogeneity of metastatic CRC – as evidenced by a representation of somatic variants and CNAs analogous to that found in clinical datasets of CRC metastases – and showed high intra-pair

genetic and transcriptional similarity. Moreover, PDXTs preserved their copy number and clonal architecture and maintained consistent transcriptomic profiles over time, at least through the first 12 passages, indicating overall stability and usability during this time frame.

While we have not thoroughly examined whether this concordance extends to parental tumors in donor patients, a recent study of mutation, copy number, gene fusion, and transcriptomic profiles in several tumor types, including 65 pairs of CRC original samples versus matched PDXs, investigated the extent of consistency between the pre-implantation human tumors and the derived xenografts²⁸. We acknowledge the possibility that some patient tumor derivatives may diverge from originating samples due to selection bottlenecks and/or evolutionary drift. However, we believe that the molecular profiles displayed by individual models accurately reflect those of spontaneous tumors in the general population, and we regard our collection as an illustrative census of metastatic CRC as a whole. It is important to note that our study was not designed to prospectively guide human care in patients, an approach that would necessitate tumors in patients to have perfect equivalents in culture and mice to reliably return results to the clinic⁵⁸. Therefore, XENTURION should be viewed primarily as a resource for population-level, adequately powered preclinical cancer research rather than a translational platform leading to direct diagnostic or predictive applications for patients.

It is commonly assumed that tumoroids may be used to shortlist drug candidates before in vivo validation, but their reliability in anticipating xenograft results remains to be established¹³. The vast number of matched PDXT-PDX pairs developed in XENTURION enabled performing correlations with an adequate statistical power, which facilitated the formal assessment of the accuracy of PDXTs in predicting cetuximab response in the corresponding PDXs. To our knowledge, this is the first large-scale drug efficacy study in which a systematic comparison of therapeutic response between PDXT-PDX pairs was attempted, and the first report gauging the diagnostic ability of PDXTs in informing subsequent steps of in vivo experimentation. We also found that the effect of pharmacologic versus genetic inactivation of EGFR on tumoroid viability was similar. Therefore, mapping cancer dependencies by methodical gene knockout in tumoroids is expected to deliver results comparable to those achieved by drug-mediated perturbation; this should help prioritize pharmaceutical development pipelines for those drug-orphan targets that, when deleted, drastically impair tumoroid growth⁵¹.

Our PDXT pharmacologic characterization uncovered experimental drugs with therapeutic potential. We reasoned that some cetuximab-induced genes might contribute to adaptive tolerance to EGFR inhibition, and blockade of their protein products should enhance cetuximab sensitivity. With this premise, genes concordantly

and specifically upregulated by cetuximab in PDXs and PDXTs were prioritized based on tractability. Potential targets were further selected according to the extent to which their inhibition impacted tumoroid viability, and based on this ranking three candidates (NUAK2, ULK1, and HDACs) were shortlisted. Accordingly, their neutralization deepened response to cetuximab. Notably, all three targets are involved in autophagy, a stress-induced survival pathway during which vesicles called autophagosomes engulf damaged organelles and unfolded proteins and deliver them to the lysosome for degradation⁵³. In particular, NUAK2 and ULK1 participate in the formation of autophagic vesicles^{53,59}, and HDACs control the fusion of autophagosomes to lysosomes⁶⁰. Although we have not formally documented induction of autophagy after cetuximab treatment, it is tempting to speculate that autophagy may be an alternate survival strategy deployed by CRC tumors to counteract the growth-inhibitory effect of EGFR inactivation, and autophagy inhibitors may cooperate with cetuximab to achieve deeper tumor regressions.

Results gathered from our experiments also highlight the limitations of XENTURION. The minimal composition of the growth medium (which contained EGF as the sole growth factor) was instrumental to standardizing culture conditions and sufficient to ensure the growth of most tumoroids, but favored the establishment of EGF-dependent models – such as those derived from metastases of left-colon primary tumors – and disfavored that of models with a higher reliance on exogenous WNT signals – namely, those with *CTNNB1* (encoding β -catenin) rather than *APC* mutations. In the same vein, viability assays with cetuximab were biased by the need to remove EGF from the medium to avoid antibody competition for the same receptor binding sites. This procedure was conducive to some ‘false positives’ in PDXTs, as exemplified by the observed sensitivity of *ERBB2*-amplified tumoroids to cetuximab, which was not confirmed in matched PDXs. In this case, it is arguable that the poor culture milieu experienced by PDXTs made them more susceptible to EGFR inhibition than corresponding xenografts in mice, which likely were exposed to survival signals conveyed by the host. In general, the impact of culture media composition on tumoroid ability to predict therapeutic responses is substantial⁶¹, and additional work is needed to define cocktails of growth factors with a proper balance between the necessity of methodological synthesis and that of coping with idiosyncratic model characteristics.

Another inherent drawback of serially passaged PDXs and long-term cultured tumoroids is their inability to retain human stromal and immune components, which hinders the assessment of the tumor microenvironment’s contribution to tumor growth and drug response^{3,6}. Various attempts have been made to develop more comprehensive models that preserve the overall tumor cellular contexture and architecture, including cocultures of tumoroids with autologous peripheral blood lymphocytes⁶² or carcinoma-associated fibroblasts^{63,64}, human air–liquid interface cohesive units⁶⁵, and thin-slice tumor fragments⁶⁶. While these models offer valuable insights, they involve complex methodologies that are not easily scalable to population-level approaches, and the complete functionality of tumor-immune interactions is yet to be fully established². Furthermore, the substitution of human stroma with murine counterparts in PDXs complicates model assignment to molecular subtypes derived from human whole-tumor transcriptomes, in which the abundance of stromal and immune transcripts influences transcriptional classification^{34,35,39,67}. This limitation is evident in the observed systematic loss of classification for the CMS4 subtype, which is mainly sustained by transcripts of stromal origin.

In conclusion, we have implemented protocols for sharing XENTURION models and associated data responsibly with the scientific community, while protecting patient confidentiality and the right to withdraw informed consent. We have also planned the development of a user-friendly web portal that will provide open access to the

molecular and biological characteristics of the models and visualization tools. In conclusion, XENTURION is a rich resource that augments and integrates existing genomic, transcriptomic and functional datasets of CRC tumoroid collections. Being open to external parties, this resource is expected to yield fertile ground for catalyzing independent preclinical cancer research and fostering the discovery process.

Methods

Specimen collection and annotation

Tumor samples were obtained from donor patients treated by liver metastasectomy at the Candiolo Cancer Institute (Candiolo, Torino, Italy), Ospedale Mauriziano Umberto I (Torino), Città della Salute e della Scienza di Torino – Presidio Molinette (Torino), and Grande Ospedale Metropolitano Niguarda (Milano, Italy). All patients provided informed consent, including for the collection of sex and age information. The sex of donor patients was determined based on self-report and was not considered in the analysis of molecular data or in the correlations between pharmacologic response and molecular profiles in patient-derived models. Samples were procured and the study was conducted under the approval of the Review Board of the Fondazione del Piemonte per l’Oncologia FPO - IRCCS (PROFILING protocol No. 001-IRCC-00IIS-10, version 11.0, updated July 13, 2022). Clinical and pathological data were entered and maintained in our prospective database. The deidentified clinical information in this study is published in accordance to the ethics guidelines of the PROFILING protocol.

DNA and RNA extraction, sgRNA PCR amplification, Sanger sequencing, and DNA fingerprinting

Total DNA and RNA were extracted using the Maxwell[®] Instrument (Promega) following manufacturer’s instructions. *EGFR*-amplified products were obtained by PCR using the following primers: 5′-CAG-GAGGTGGCTGGTTATGT-3′ and 5′-TTCTCCGAGGTGGAATTGAG-3′. Sanger sequencing was performed by using the following primer: 5′-TTCTCCGAGGTGGAATTGAG-3′.

DNA fingerprinting was performed using a MassARRAY Sequenom instrument and the Myriapod genotyping panel (Diatech Pharmacogenomics), which covers 24 human SNPs. The genetic identity of PDX and tumoroid samples was cross-checked across matched models and against pre-derivation surgical material as a reference. In instances where two or more homozygous SNPs showed discordance, the samples were excluded from further analysis.

To obtain bulk RNA-seq data, RNA was extracted using miRNeasy Mini Kit (Qiagen), according to the manufacturer’s protocol. The quantification and quality analysis of RNA was performed on a Bioanalyzer 2100 (Agilent), using RNA 6000 Nano Kit (Agilent).

Analysis of mutant variants

Targeted sequencing was performed on an Illumina NovaSeq 6000 instrument by IntegraGen SA. Paired-end 2x100bp reads were obtained, aiming at ~500x depth for each sample on the targeted regions (402.4 kbp). The panel (Twist Bioscience) covered exons of 116 genes (Supplementary Data 10) from a manually curated list of recurrently mutated drivers in CRC. Initial quality check (QC) was performed with FastQC (v0.11.9) by IntegraGen; for PDX samples, murine reads were filtered using Xenome (v1.0.0) with default parameters, after building k-mer indexes for the human genome (GRCh38, downloaded from <https://gdc.cancer.gov/about-data/gdc-data-processing/gdc-reference-files>) and murine genome (mm10, obtained from iGenomes). The GATK Best Practices Workflow⁶⁸ for somatic mutation calling was followed to perform mutation calling with Mutect2 (bwa v0.7.17-r1188 - parameters -K 100000000 -Y, GATK 4.1.4.0); alignment was performed versus GRCh38; alignment metrics were gathered with picard CollectHsMetrics (Supplementary Data 10). dbSNP (for quality recalibration, downloaded from NCBI, <ftp://ftp.ncbi.nih.gov/snp/>)

[organisms/human_9606/VCF/All_20180418.vcf.gz](https://www.ncbi.nlm.nih.gov/genomes/human_9606/VCF/All_20180418.vcf.gz)) and Gnomad (release 2.1.1) were used as external references for common human polymorphisms. The resulting list of filtered mono-allelic mutations was annotated using the Personal Cancer Genome Reporter (PCGR, version 0.9.1)⁶⁹. To avoid germline contamination, only coding mutations found in tiers ≤ 3 were kept for further analyses. TCGA and MSK-IMPACT mutational data was downloaded from https://www.cbioportal.org/study/clinicalData?id=crc_msk_2017 and https://www.cbioportal.org/study/summary?id=coadread_tcga_pan_can_atlas_2018 - Mutated_Genes.txt. To compare mutational landscapes between PDXs and PDXT, we considered mutations with $AF > 0.05$.

Whole exome sequencing was conducted on Illumina NovaSeq by Biodiversa SRL using the IDT xGen Exome Hyb Panel v2. Paired-end 2x150bp reads were obtained, aiming at $\sim 100\times$ on-target depth (34 Mbp, 19,433 genes). Mutation calling and annotation were performed with the same pipeline as for targeted sequencing, with an additional filtering step to refine Mutect2 results. Specifically, we implemented a custom script that exploits BLAT (v. 35x1)⁷⁰ to verify whether reads can be found that include both the candidate variant (either an SNV or an indel) and its surrounding 20 flanking bases in the absence of any gap or further mismatch. Variants lacking supporting reads were discarded from further analysis.

Copy number profiles and LOH analysis

Low-pass whole genome sequencing was performed on Illumina NovaSeq S4 instrument by Biodiversa SRL (Supplementary Data 11). Paired-end 2x150bp reads were obtained, aiming at 0.65x depth for each sample. Initial QC was performed with FastQC (v0.11.8); for PDX samples, murine reads were filtered using Xenome (v1.0.0) with the same procedure described for targeted sequencing. Total or human classified reads were aligned versus GRCh38 with bwa (v0.7.17-r1188 -parameters -K 100000000 -Y) following GATK best practices; then, duplicates were marked using picard (2.18.25). Alignment metrics were gathered with samtools (v1.9) flagstat and picard CollectWgsMetrics (Supplementary Data 11). Segmented fold changes were obtained with QDNAseq (v1.22.0)⁷¹ with a bin size of 15 kb (annotations obtained from QDNAseq.hg38), using default parameters and pairedEnds=TRUE. Before computing correlations, a pseudocount of 1 was added to all fold changes to compute \log_2 ; a pseudocount of 0.01 was used for visualization. \log_2 values with a pseudocount of 1 in .seg format were used as input for the GISTIC2.0 module in GenePattern (<https://cloud.genepattern.org>, default parameters and TRHuman_Hg38.UCSC.add_miR.160920.refgene.mat, Gistic v2.0.23). TCGA Gistic output (specifically all_thresholded.by_genes.txt) was downloaded from the GDCL (https://gdc.cancer.gov/about-data/publications/coadread_2012); for MSK-IMPACT, the file with segmented signals was downloaded from cBioPortal (https://www.cbioportal.org/study/clinicalData?id=crc_msk_2017) and GISTIC was run as previously described.

For LOH analysis, whole exome sequencing reads from early- and late-passage PDXs, PDXs and their matched normal DNA obtained from liver tissue were aligned, and duplicates were filtered as described above. The resulting read set was analyzed with Sequenza (ref v3.0.0) using default parameters and 50 base pairs bins. Poorly mappable regions, as defined by the Broad Institute (https://storage.googleapis.com/genomics-public-data/resources/broad/hg38/v0/wgs_calling_regions.hg38.interval_list), were excluded from the analysis. Sequenza outputs were filtered to collect only segments with a B allele frequency (BAF) of 0, and BEDtools (v2.27.1) was used to define overlapping segment regions across samples. The regions obtained from segment overlapping were then assigned to three categories: (1) Gained LOH: regions with BAF = 0 in the early-passage PDX but different from 0 in the parental PDX, or regions with BAF = 0 in the late-passage PDX but different from 0 in its matched early-passage

counterpart; (2) Common LOH: regions with BAF = 0 at both analyzed pairs; (3) Errors: regions with BAF = 0 in the parental PDX but different from 0 in the early-passage PDX, or regions with BAF = 0 in the early-passage PDX but different from zero in its matched late-passage counterpart. The rest of the mappable genome was defined as 'No LOH', representing regions with BAF different from 0 in both analyzed pairs. To visualize results, we binned the genome at a fixed segmentation size. In case of partial overlap of a region with a bin, only the largest intersection was considered. The segmentation size was set at 100kb to ensure a good representation of small events.

Analysis of subclonal heterogeneity

Differences in clonal composition of early- and late-passage PDXs, as well as matched PDXs, were evaluated using PyClone-vi (v. 0.1.3)³². This tool makes use of copy-number and single nucleotide information to infer the number of clonal expansions coexisting within a tumor. To generate the input for PyClone-vi, we developed a custom script to merge the SNVs called by Mutect2 and the CNAs inferred by Sequenza. The output from PyClone-vi included the estimated number of clones (referred to as clusters) in each sample, the list of mutations supporting each cluster, and a set of supplementary annotations. Among these annotations, the 'cluster_assignment_prob' (posterior probability for each mutation being assigned to a specific cluster) was used as a proxy for cluster reliability.

Gene expression analyses

Quality control checkpoints. Total RNA was processed for RNA-seq analysis with the TruSeq RNA Library Prep Kit v2 (Illumina) following manufacturer's instructions, and sequenced on a NextSeq 500 system (Illumina) by Biodiversa SRL. Single-end 151 bp reads were obtained, aiming at 20 M reads for each sample. Read counts were obtained using an automated pipeline (<https://github.com/molinerisLab/StromaDistiller>), that uses a hybrid genome composed of both human and mouse sequences to exploit the aligner ability to distinguish between human-derived reads, representing the tumor component, and mouse-derived reads, representing the murine host contaminating RNA material. Reads were aligned using STAR⁷² (version 2.7.1a, parameters --m outSAMunmapped Within --outFilterMultimapNmax 10 --outFilterMultimapScoreRange 3 --outFilterMismatchNmax 999 --outFilterMismatchNoverLmax 0.04) versus this hybrid genome (GRCh38.p10 plus GRCm38.p5hg38 with Gencode version 27 and mouse GRCm38 with Gencode version 16, indexed with standard parameters and including annotation information from the GENCODE 27 plus m16 comprehensive annotation). Aligned reads were sorted using sambamba⁷³ (version 0.6.6) and only non-ribosomal reads were retained using split_bam.py⁷⁴ (version 2.6.4) and rRNA coordinates obtained from the Gencode annotation and RepeatMasker track downloaded from UCSC genome browser hg38 and mm10. featureCounts⁷⁵ (version 1.6.3) was run with the appropriate strandness parameter (-s 2) to count the non-multi-mapping reads falling on exons and reporting gene-level information (-t exon -g gene_name) using combined Gencode basic gene annotation (27 plus m16).

Sequencing data was available for 1015 samples, but different filtering criteria resulted in 999 samples surviving quality checks. These criteria included: (i) number of total reads ≥ 15 M; (ii) reads assigned to genes by feature counts $\geq 60\%$; (iii) reads assigned to human genes over the total of assigned reads $\geq 30\%$. By applying these filters, only samples with at least 5 M human reads were considered for analysis. To remove samples with lymphomatous characteristics³⁵, 2 criteria were applied: (i) Principal Component analysis of expression data (samples with $PC2 \geq 30$ were discarded); (ii) computation of a sample-level score for a leukocyte expression signature³⁴, averaging FPKM values for all the signature genes (samples with an average leukocyte signature ≥ 48 were discarded). Positivity for either criterion flagged samples as

lymphomatous and excluded them from analysis. The overall concordance of the PC score with the leukocyte expression signature is shown in Supplementary Fig. 19C.

Samples were sequenced in five different batches. This did not largely affect sample separation based on Principal Component analysis (Supplementary Fig. 19A). However, when possible, batch correction was applied in downstream differential analyses. Variance stabilized expression and robust FPKM values were obtained using DESeq2⁷⁶ (version 1.26.0), tmm using edgeR (version 3.28.1) starting from the read counts assigned to human genes only.

Differential expression analysis. Differentially expressed genes (DEGs) between original tumors, PDXs and PDXTs were obtained using R package DESeq2 (v1.26.0) with the formula “-batch + type + sample”. By applying this formula, ‘batch’ was used to correct for sequencing batches; ‘type’ specified sample origin (surgical specimen, PDX, or tumoroid); and ‘sample’ was an identification tag assigned to each original tumor (sample was added in the formula to obtain DEGs between sample types, taking into account tumor identity). Genes with more than 5 reads in only 1 sample were removed before testing for differential expression. DEGs were identified using $|LFC| \geq 0.5849625$ and adjusted P values < 0.05 . Samples were selected starting from PDXTs that had passed the validation process and their paired PDXs and HLMs. The obtained DEGs were used to perform GO enrichment analysis with R libraries ClusterProfiler^{77,78} (v3.14.3), DOSE⁷⁹ (v3.12.0), msigdb⁸⁰ (v7.4.1), and enrichplot (v1.6.1). Graphical representations of GO Biological Process enrichments were obtained with REVIGO⁸¹, which was manually run online on 05/12/22 with the list of GO terms with adjusted P values < 0.05 as input and selecting ‘small’ as output size. The final plots were obtained by manual highlighting of a subset of relevant terms with ggplot.

DEGs between untreated and cetuximab-treated samples were obtained using the formula “-sample + treat” for PDXTs and “-sample + time + treat” for PDXs; ‘treat’ indicated if sample was treated or untreated; ‘time’ indicated time of PDX exposure to treatment (three days or six weeks). The list of significant DEGs in PDXTs was refined by successive filters (Supplementary Fig. 16 and Supplementary Data 7), considering only: (i) genes upregulated by cetuximab in PDXTs (\log_2 fold change > 0); (ii) genes also upregulated by cetuximab in responsive PDXs (\log_2 fold change > 0 and adjusted P value < 0.05); (iii) genes with no significant expression changes (adjusted P value ≥ 0.05) after exposure of cetuximab-resistant PDXs to antibody treatment; (iv) genes with a baseMean, reported by DESeq2, $>$ than their overall median. The list of resulting gene symbols was annotated for tractability considering buckets 1–7 in Behan et al.⁵⁰ and used as input in the Search Interaction form of the Drug-Gene Interaction Database (www.dgidb.org) on 26/03/2021.

Number of models and replicates used in comparisons. The transcriptomic dataset used for differential gene expression analyses encompassed 21 surgical specimens from donor patients, with 1 replicate for each sample; 119 PDXs from which PDXTs were successfully derived and validated (1 replicate for 115 models, 2 replicates for 4 models); 49 PDXs from which PDXT early derivation or validation had failed (1 replicate for 42 models, 2 replicates for 7 models); and 124 validated PDXTs (1 replicate for 49 models, 2 replicates for 75 models). The gene expression correlation analysis in the subset of 79 ‘super-matched’ PDX-PDXT pairs was performed with one replicate for each sample. The larger analysis involving 116 PDX-PDXT pairs comprised a total of 308 data points, including replicates. For the PDX data, this included 1 replicate for 112 models and 2 replicates for 4 models; for PDXT data, there was 1 replicate for 44 models and 2 replicates for 72 models. The number of replicates depended on the availability of quality-checked RNA material in sufficient quantities for RNAseq library preparation and sequencing QC.

Transcriptional subtype assignment. CMS subtypes were called on the vsd matrix for PDXTs, PDXs and HLMs separately, using R package CMScaller⁸² (v2.0.1) with parameters FDR = 0.05 and RNAseq = TRUE. CRIS subtypes were also called on the vsd matrix with the R package CRISclassifier³⁵ (v1.0.0).

Hierarchical clustering. Hierarchical clustering (method = ‘complete’, distance metric 1 - Pearson correlation) was performed on vsd expression data, keeping replicate samples as separate entities. Filters were applied to eliminate low-expressed genes and to maintain those with highly variable expression; specifically, genes with average expression across samples larger than the overall median of averages and the top 10% genes with higher standard deviation were analyzed.

Inference of tumor’s primary tissue of origin. Inference of tumor’s primary tissue of origin was obtained with CUP-AI-Dx (<https://github.com/TheJacksonLaboratory/CUP-AI-Dx>, docker yuz12012/ai4cancer:product)³⁷ with \log_2 tmm with a pseudocount of 1 as expression values.

Patient-derived tumoroid cultures

Tumoroids of CRC liver metastases were obtained from PDX explants or directly from surgical resections of donor patients. Tumor specimens (0,5 cm×0,5 cm) were chopped with a scalpel and washed with PBS. After centrifugation, the final cell preparation was embedded in Matrigel® (Corning) or Cultrex Basement Membrane Extract (BME Type II or Ultimatrix RGF BME, R&D Systems) and dispensed onto 24-well plates (Corning). After 10–20 minutes at 37 °C, culture medium was added. Complete tumoroid medium composition was the following: Dulbecco’s modified Eagle medium/F12 supplemented with penicillin-streptomycin, 2 mM L-glutamine, 1 mM n-Acetyl Cysteine, B27 (Thermo Fisher Scientific), N2 (Thermo Fisher Scientific), and 20 ng/ml EGF (Sigma-Aldrich). Tumoroids were tested for Mycoplasma and maintained at 37 °C in a humidified atmosphere of 5% CO₂. Periodic checks of sample identity with the original human specimen (liver metastasis and, when available, normal liver) were performed using a 24 SNP custom genotyping panel (Diotech Pharmacogenetics), and results were analyzed using the MassARRAY Analyzer 4 (SEQUENOM® Inc, California). Culture expansion and biobanking were managed using the Laboratory Assistant Suite⁸³.

Viability assays

Pharmacologic experiments were performed in 96-well plates with a thin layer of BME in each well. PDXTs were washed with PBS, incubated with trypsin-EDTA solution for 5 minutes at 37 °C and vigorously pipetted to obtain a single cell suspension. Cells were seeded in 2% BME culture medium in the absence of EGF. After 1–2 days from seeding, PDXTs were treated with the modalities indicated in the figure legends. Cetuximab was provided by Merck; HTH-02-006 was purchased from Aobious; all other small-molecule inhibitors were purchased from Selleckchem. Cell viability was measured by ATP content using the Cell Titer-Glo luminescent assay kit (Promega). For cell imaging, bright-field images were acquired on a Cytation 3 cell imaging multi-mode reader (BioTek Instruments) with a 4x Olympus objective. Images were mounted by stitching together 12 different fields of view in order to completely cover each well of the plate. Images were then processed according to a custom-made Fiji script⁸⁴ to segment tumoroid areas. Edge detection algorithms were used to get rid of the non-uniform brightness resulting from illuminating a multi-well plate, followed by a thresholding step and a morphological filling. Segmented objects were then filtered according to their size and aspect ratio and total tumoroid area was used as a proxy for growth. Data dispersion was assessed by applying a coefficient of variation (CV), calculated as the ratio of the standard deviation of untreated or treated cells to the average signal of untreated cells. Experiments were

excluded when none of the three cell densities tested (1250, 5000 or 20,000 cells/well in a 96-well format) for at least one of the two readouts (ATP content and longitudinal cell imaging) displayed CV values lower than 0.25.

CRISPR-Cas9 gene editing and dependency assays

PDXTs were transduced with a Cas9-expressing pKLV2-EF1a-BsdCas9-W lentiviral vector (Addgene) and selected with 10 µg/ml blasticidin (Thermo Fisher Scientific). sgRNAs were cloned into the pKLV2-U6gRNAs(BbsI)-PGKpuro2AZsG-W lentiviral vector (Addgene). sgRNA sequences were designed to target the following genes: i) *EGFR* (sgEGFR#1, GATAAGACTGCTAAGGCAT; sgEGFR#2, GCAAATAAAACC GGACTGA); ii) the essential gene *PLK1* (GCGGACGCGGACCAAGG); the non-essential gene (*CYP2A13*, GTCACCGTGCGTCCCCGG). After transduction with the sgRNA vectors, Cas9-expressing PDXTs were seeded at 5000 cells/well in 96-well plates in the presence of blasticidin and 2 µg/ml puromycin (Sigma Aldrich) and cultured for seven days. Endpoint cell viability was measured using the Cell Titer-Glo luminescent assay kit (Promega) and normalized to day one. A KO score was calculated using the following formula:

$$\frac{(\text{ATP } EGFR\text{-KO} - \text{ATP } PLK1\text{-KO})}{(\text{ATP } CYP2A13\text{-KO} - \text{ATP } PLK1\text{-KO})}$$

Where ATP *EGFR*-KO indicates the ATP content value of *EGFR*-KO cells, ATP *PLK1*-KO indicates the ATP content value of cells in which the *PLK1* essential gene was deleted, and ATP *CYP2A13*-KO indicates the ATP content value of cells in which the *CYP2A13* non-essential gene was deleted. Only PDXTs in which endpoint viability values after *PLK1* KO were at least 30% less than those of *CYP2A13* KO cells were included in the analyses.

Western blot analysis

Four days after sgRNA transduction, PDXTs were harvested and total cellular proteins were extracted with boiling Laemmli buffer (1% SDS, 50 mM Tris-HCl pH 7.5, 150 mM NaCl). After sonication, total proteins were quantified using the BCA Protein Assay Reagent Kit (Thermo Fisher Scientific), electrophoresed on precast polyacrylamide gels (Invitrogen), and transferred onto nitrocellulose membranes using a Trans-Blot Turbo Blotting System (Biorad). Membrane-bound antibodies were detected by the enhanced chemiluminescence system (Promega). Primary antibodies were rabbit anti-EGFR (clone D38B1, Cell Signaling Technology #4267, 1:1,000 dilution) and mouse anti-vinculin (clone hVIN-1, Sigma-Aldrich, V9131, 1:2,500 dilution).

PDX studies

Tumor material not required for histopathologic analysis was collected and placed in Medium 199 (Thermo Fisher Scientific) supplemented with 200 U/ml penicillin, 200 µg/ml streptomycin, and 100 µg/ml levofloxacin (all from Sigma-Aldrich). Each sample was cut into 25- to 30-mm³ pieces in antibiotic-containing medium; tumor fragments were then implanted and propagated in 6-week-old male and female NOD-SCID mice purchased from Charles River Laboratories (Italy). All procedures using live animals were reviewed and approved by the Candiolo Cancer Institute Institutional Animal Care and Use Committee (IACUC) and by the Italian Ministry of Health (authorization 37/2022-PR) and complied with all relevant ethical regulations. Mice with established tumors (average volume ~300 mm³) were randomized and treated with the modalities indicated in the figures. Vehicle compositions were the following: 10% DMSO and 5% dextrose for HTH-02-006; 5% Tween-80 and 5% polyethylene glycol (PEG) 400 in PBS for SBI-0206965; and 25% hydroxypropyl-β-cyclodextrin, 5% DMSO, and 45% PEG 400 for vorinostat. Tumor size was evaluated once weekly by caliper measurements, and the approximate volume of the mass was calculated using the formula $\frac{4}{3}\pi (d/2)^2 D/2$, where *d* is the minor tumor axis and *D* is the major tumor axis. The maximum tumor diameter approved by the IACUC and the Italian Ministry of Health (10 mm) was not exceeded. Sex was not considered in the study design

as systematic population-level studies with cetuximab have shown no significant differences in response between male and female mice^{14–16}.

The TGI score was defined as the difference in the relative growth (RG) at three weeks for tumors in the treated arm compared to the placebo arm, corrected by the placebo RG, and expressed as a percentage:

$$\text{RG cetuximab} = (C3 - C0)/C0 \quad (1)$$

$$\text{RG placebo} = (P3 - P0)/P0 \quad (2)$$

$$\text{TGI} = [(\text{RG cetuximab} - \text{RG placebo})/\text{RG placebo}] * 100 \quad (3)$$

Where C3 and C0 represent the median tumor volume in mice treated with cetuximab for three weeks and the median tumor volume at the start of treatment, respectively, while P3 and P0 represent the median tumor volume in the placebo arm after three weeks of treatment and the median tumor volume at the start of treatment, respectively. If cetuximab treatment data were available for two independent PDX propagations of the original tumor in the donor patient, we averaged the resulting TGIs. This formula yields values closer to 0 for tumors whose growth is not significantly affected by treatment, and negative values for responsive tumors, accounting for the specific growth rate of each untreated tumor.

Results were considered interpretable when a minimum of four mice per treatment group reached the prespecified endpoints (at least 3 weeks on therapy or development of tumors with the largest diameter ≥ 10 mm). In vivo procedures and related biobanking data were managed using the Laboratory Assistant Suite⁸³.

Statistics and reproducibility

No statistical method was used to predetermine the sample size. For experiments in mice, guidance was provided by our previous experience with different PDX models^{16,17}, and sample size conformed to PDX minimal information standards⁵⁴. Tumor-bearing mice were randomized before treatment by allocating mice to alternate treatment groups using the Laboratory Assistant Suite⁸³. The investigators were not blinded to allocation during experiments and outcome assessment.

For comparisons between PDXs and PDXTs at different omics levels, all samples meeting standard DNA and RNA quality and quantity criteria for sequencing were used. Nineteen cases were excluded due to incorrect fingerprinting, four cases were diagnosed as lymphomas based on histopathologic evaluation, and one case was excluded for technical reasons (deterioration of archived material). One PDXT model with expression levels poorly correlating with the rest of the cohort and unclear histology of the tumor of origin was excluded from pharmacologic analyses. Standard QC was performed on all sequencing data. Approximately 1% of RNA sequencing samples were filtered out based on read number and signs of lymphomatous infiltration. For *EGFR* KO experiments, only PDXTs where endpoint viability values after *PLK1* (essential gene) KO were at least 30% lower than those of *CYP2A13* (non-essential gene) KO cells were included in the analyses.

The number of biological (nontechnical) replicates for each experiment is reported in the figure legends, alongside the adopted statistical tests and metrics. For comparisons between two groups, statistical analyses were performed using two-tailed *t* tests, applying Welch's correction for unpaired tests. To compare similarity estimates between tumoroids and xenografts for matched and unmatched PDX and PDXT models, two-tailed Mann-Whitney tests were applied. For experiments with more than two groups or when comparing dose-response curves in tumoroids, one-way ANOVA was used. When comparing matched data, repeated measures one-way ANOVA was performed. In case of multiple testing, the Šidák's or Benjamini-

Hochberg multiple comparison corrections were implemented. Odds ratios were calculated using multivariate logistic regression models. Correlations were calculated by Pearson's coefficients. The reported confidence intervals are at 95%; IQR intervals are between the first and the third quartile. Error bars indicate the standard error of the mean unless indicated otherwise. Statistical analyses were performed using GraphPad Prism (v9.0) and R (v3.6.3), including base R packages and the `precrec` R package (v0.12.9).

Figure preparation

Unless otherwise specified, graphs and data visualizations were generated using GraphPad Prism and the R packages `ggplot2` (v3.3.0), `heatmap` (v1.0.12), `ComplexHeatmap` (v2.2.0), `sjPlot` (2.8.10) and `circize` (v0.4.15). Gene copy number and LOH heatmaps (Figs. 3B and 4B, 4C, Supplementary Fig. 9B, C, and Supplementary Figure 10A, B) were generated using `python3/matplotlib/clustermap` from `seaborn` (v3.7.3/3.4.3/0.0.0). The Sankey plot in Fig. 5C was generated using the package `networkD3` (v0.4) and its function `sankeyNetwork`. Parts of Fig. 1A were drawn using adaptations of open-access pictures released under Creative Commons Attribution Licenses: Servier Medical Art (https://smart.servier.com/smart_image/mouse/), https://smart.servier.com/smart_image/multi-well-plate-ov/, https://smart.servier.com/smart_image/complete-overview-digestive-apparatus/, and https://smart.servier.com/smart_image/overview-cancer-cell-smart/), licensed under CC BY 4.0 International (<https://creativecommons.org/licenses/by/4.0/>); DataBase Center for Life Science (<https://doi.org/10.7875/togopic.2018.23>), licensed under CC BY 4.0 International; and Bioicons contributions by Marcel Tisch (<https://bioicons.com/?query=drug> and <https://bioicons.com/?query=organoid>), licensed under CC0 1.0 Universal (<https://creativecommons.org/publicdomain/zero/1.0/>).

Reporting summary

Further information on research design is available in the Nature Portfolio Reporting Summary linked to this article.

Data availability

The sequencing data generated in this study have been deposited in the European Genome-phenome Archive (EGA) under the following accession numbers: [EGAS00001006697](https://ega-archive.org/studies/EGAS00001006697) for targeted DNA sequencing; [EGAS00001006696](https://ega-archive.org/studies/EGAS00001006696) for low-pass whole genome sequencing; [EGAS00001007024](https://ega-archive.org/studies/EGAS00001007024) for RNA sequencing of tumoroids; [EGAS00001006492](https://ega-archive.org/studies/EGAS00001006492) for RNA sequencing of PDXs; [EGAS00001006746](https://ega-archive.org/studies/EGAS00001006746) for RNA sequencing of original human samples; [EGAS00001006601](https://ega-archive.org/studies/EGAS00001006601) for RNA sequencing of cetuximab-treated and untreated tumoroids; [EGAS00001006973](https://ega-archive.org/studies/EGAS00001006973) for RNA sequencing of cetuximab-treated and untreated PDXs. All the above datasets include more samples than those specifically analyzed in this study. To protect patient privacy, as required by law, access to the raw data deposited in EGA is controlled by a Data Access Committee (DAC) represented by E.G. and L.T. All researchers can obtain access by contacting EGA, which will notify the DAC of the access request. The DAC will honor the requests within approximately 2 weeks and will determine the length of permitted access. Processed expression levels and raw read counts are publicly available in GEO (GSE204805) [<https://www.ncbi.nlm.nih.gov/geo/query/acc.cgi?acc=GSE204805>]. Supplementary Data 10 reports the results of DNA-targeted sequencing. Supplementary Data 11 reports the GISTIC analysis of low-pass whole genome sequencing data. Supplementary Data 12 lists the samples subjected to DNA-targeted sequencing and low-pass whole genome sequencing. Supplementary Data 13 lists the samples subjected to RNA sequencing. Supplementary Data 14 reports QC summaries of whole exome sequencing data for PDX, early-passage PDX, and late-passage PDX trios. Drug responses are presented in Supplementary Data 6. All codes for accessing other intermediate analysis data and reproducing bioinformatics-related main figure panels were consolidated into a single GitHub repository,

referred to in Zenodo (<https://zenodo.org/doi/10.5281/zenodo.13378796>). The remaining data are available within the Article, Supplementary Information or Source Data file. PDX and PDXT models described in this study are available for research purposes from A.B. and L.T. under a material transfer agreement (MTA) with the Candiolo Cancer Institute. According to patient informed consent, living propagatable material is not shareable with for-profit entities. Source data are provided with this paper.

Code availability

All pipelines used to parse and analyze DNA and RNA sequencing data were developed and run with `snakemake`⁸⁵ (v5.4.0). Codes are available at the following repositories: (i) <https://github.com/vodkatad/snakegatk> (targeted sequencing and low-pass whole genome sequencing alignment and GATK best practices); (ii) https://github.com/vodkatad/RNASeq_biod_metadata (RNAseq overall QC and metadata management); (iii) https://github.com/vodkatad/biodiversa_DE (RNA-seq differential analysis); (iv) <https://github.com/vodkatad/bioanca> (overall comparative analyses).

References

- van de Wetering, M. et al. Prospective derivation of a living organoid biobank of colorectal cancer patients. *Cell* **161**, 933–945 (2015).
- van Renterghem, A. W. J., van de Haar, J. & Voest, E. E. Functional precision oncology using patient-derived assays: bridging genotype and phenotype. *Nat. Rev. Clin. Oncol.* **20**, 305–317 (2023).
- Bose, S. et al. A path to translation: how 3D patient tumor avatars enable next generation precision oncology. *Cancer Cell* **40**, 1448–1453 (2022).
- Sasaki, N. & Clevers, H. Studying cellular heterogeneity and drug sensitivity in colorectal cancer using organoid technology. *Curr. Opin. Genet. Dev.* **52**, 117–122 (2018).
- Avolio, M. & Trusolino, L. Rational treatment of metastatic colorectal cancer: a reverse tale of men, mice, and culture dishes. *Cancer Discov.* **11**, 1644–1660 (2021).
- Zanella, E. R., Grassi, E. & Trusolino, L. Towards precision oncology with patient-derived xenografts. *Nat. Rev. Clin. Oncol.* **19**, 719–732 (2022).
- Flood, M. et al. Organoids as a robust preclinical model for precision medicine in colorectal cancer: a systematic review. *Ann. Surg. Oncol.* **29**, 47–59 (2022).
- Betge, J. & Jackstadt, R. From organoids to bedside: advances in modeling, decoding and targeting of colorectal cancer. *Int. J. Cancer* **152**, 1304–1313 (2023).
- Vlachogiannis, G. et al. Patient-derived organoids model treatment response of metastatic gastrointestinal cancers. *Science* **359**, 920–926 (2018).
- Schumacher, D. et al. Heterogeneous pathway activation and drug response modelled in colorectal-tumor-derived 3D cultures. *PLoS Genet.* **15**, e1008076 (2019).
- Bruun, J. et al. Patient-derived organoids from multiple colorectal cancer liver metastases reveal moderate intra-patient pharmacotranscriptomic heterogeneity. *Clin. Cancer Res.* **26**, 4107–4119 (2021).
- Ooft, S. N. et al. Patient-derived organoids can predict response to chemotherapy in metastatic colorectal cancer patients. *Sci. Transl. Med.* **11**, eaay2574 (2019).
- LeSavage, B. L., Suhar, R. A., Brogiere, N., Lutolf, M. P. & Heilshorn, S. C. Next-generation cancer organoids. *Nat. Mater.* **21**, 143–159 (2022).
- Bertotti, A. et al. A molecularly annotated platform of patient-derived xenografts (“xenopatients”) identifies HER2 as an effective therapeutic target in cetuximab-resistant colorectal cancer. *Cancer Discov.* **1**, 508–523 (2011).

15. Zanella, E. R. et al. IGF2 is an actionable target that identifies a distinct subpopulation of colorectal cancer patients with marginal response to anti-EGFR therapies. *Sci. Transl. Med.* **7**, 272ra12 (2015).
16. Bertotti, A. et al. The genomic landscape of response to EGFR blockade in colorectal cancer. *Nature* **526**, 263–267 (2015).
17. Lupo, B. et al. Colorectal cancer residual disease at maximal response to EGFR blockade displays a druggable Paneth cell-like phenotype. *Sci. Transl. Med.* **12**, eaax8313 (2020).
18. Woo, X. Y. et al. Conservation of copy number profiles during engraftment and passaging of patient-derived cancer xenografts. *Nat. Genet.* **53**, 86–99 (2021).
19. Sato, T. et al. Long-term expansion of epithelial organoids from human colon, adenoma, adenocarcinoma, and Barrett's epithelium. *Gastroenterology* **141**, 1762–1772 (2011).
20. Fumagalli, A. et al. Plasticity of Lgr5-negative cancer cells drives metastasis in colorectal cancer. *Cell Stem Cell* **26**, 569–578.e7 (2020).
21. Fujii, M. et al. A colorectal tumor organoid library demonstrates progressive loss of niche factor requirements during tumorigenesis. *Cell Stem Cell* **18**, 827–838 (2016).
22. Yin, J. et al. Prognostic and predictive impact of primary tumor sidedness for previously untreated advanced colorectal cancer. *J. Natl Cancer Inst.* **113**, 1705–1713 (2021).
23. Jang, S. et al. KRAS and PIK3CA mutations in colorectal adenocarcinomas correlate with aggressive histological features and behavior. *Hum. Pathol.* **65**, 21–30 (2017).
24. Rehman, A. H., Jones, R. P. & Poston, G. Prognostic and predictive markers in liver limited stage IV colorectal cancer. *Eur. J. Surg. Oncol.* **45**, 2251–2256 (2019).
25. Matano, M. et al. Modeling colorectal cancer using CRISPR-Cas9-mediated engineering of human intestinal organoids. *Nat. Med.* **21**, 256–262 (2015).
26. Van Cutsem, E. et al. Cetuximab and chemotherapy as initial treatment for metastatic colorectal cancer. *N. Engl. J. Med.* **360**, 1408–1417 (2009).
27. Cancer Genome Atlas Network. Comprehensive molecular characterization of human colon and rectal cancer. *Nature* **487**, 330–337 (2012).
28. Sun, H. et al. Comprehensive characterization of 536 patient-derived xenograft models prioritizes candidates for targeted treatment. *Nat. Commun.* **12**, 5086 (2021).
29. Yaeger, R. et al. Clinical sequencing defines the genomic landscape of metastatic colorectal cancer. *Cancer Cell* **33**, 125–136.e3 (2018).
30. Gryfe, R. et al. Tumor microsatellite instability and clinical outcome in young patients with colorectal cancer. *N. Engl. J. Med.* **342**, 69–77 (2000).
31. Parker, T. W., Rudeen, A. J. & Neufeld, K. L. Oncogenic serine 45-deleted β -catenin remains susceptible to Wnt stimulation and APC regulation in human colonocytes. *Cancers* **12**, 2114 (2020).
32. Gillis, S. & Roth, A. PyClone-VI: scalable inference of clonal population structures using whole genome data. *BMC Bioinform.* **21**, 571 (2020).
33. Morgan, R. A. Human tumor xenografts: the good, the bad, and the ugly. *Mol. Ther.* **20**, 882–884 (2012).
34. Isella, C. et al. Stromal contribution to the colorectal cancer transcriptome. *Nat. Genet.* **47**, 312–319 (2015).
35. Isella, C. et al. Selective analysis of cancer-cell intrinsic transcriptional traits defines novel clinically relevant subtypes of colorectal cancer. *Nat. Commun.* **8**, 15107 (2017).
36. Schütte, M. et al. Molecular dissection of colorectal cancer in pre-clinical models identifies biomarkers predicting sensitivity to EGFR inhibitors. *Nat. Commun.* **8**, 14262 (2017).
37. Zhao, Y. et al. CUP-AI-Dx: a tool for inferring cancer tissue of origin and molecular subtype using RNA gene-expression data and artificial intelligence. *EBioMedicine* **61**, 103030 (2020).
38. Guinney, J. et al. The consensus molecular subtypes of colorectal cancer. *Nat. Med.* **21**, 1350–1356 (2015).
39. Calon, A. et al. Stromal gene expression defines poor-prognosis subtypes in colorectal cancer. *Nat. Genet.* **47**, 320–329 (2015).
40. Fornasier, G., Francescon, S. & Baldo, P. An update of efficacy and safety of cetuximab in metastatic colorectal cancer: a narrative review. *Adv. Ther.* **35**, 1497–1509 (2018).
41. Kavuri, S. M. et al. HER2 activating mutations are targets for colorectal cancer treatment. *Cancer Discov.* **5**, 832–841 (2015).
42. Medico, E. et al. The molecular landscape of colorectal cancer cell lines unveils clinically actionable kinase targets. *Nat. Commun.* **6**, 7002 (2015).
43. Leto, S. M. et al. Sustained inhibition of HER3 and EGFR is necessary to induce regression of HER2-amplified gastrointestinal carcinomas. *Clin. Cancer Res.* **21**, 5519–5531 (2015).
44. Peeters, M. et al. Massively parallel tumor multigene sequencing to evaluate response to panitumumab in a randomized phase III study of metastatic colorectal cancer. *Clin. Cancer Res.* **19**, 1902–1912 (2013).
45. Russo, M. et al. Tumor heterogeneity and lesion-specific response to targeted therapy in colorectal cancer. *Cancer Discov.* **6**, 147–153 (2016).
46. Sartore-Bianchi, A. et al. Dual-targeted therapy with trastuzumab and lapatinib in treatment-refractory, KRAS codon 12/13 wild-type, HER2-positive metastatic colorectal cancer (HERACLES): a proof-of-concept, multicentre, open-label, phase 2 trial. *Lancet Oncol.* **17**, 738–746 (2016).
47. Sartore-Bianchi, A. et al. HER2 positivity predicts unresponsiveness to EGFR-targeted treatment in metastatic colorectal cancer. *Oncologist* **24**, 1395–1402 (2019).
48. Zhou, X. & Agazie, Y. M. The signaling and transformation potency of the overexpressed HER2 protein is dependent on the normally-expressed EGFR. *Cell Signal.* **24**, 140–150 (2012).
49. McFarland, J. M. et al. Improved estimation of cancer dependencies from large-scale RNAi screens using model-based normalization and data integration. *Nat. Commun.* **9**, 4610 (2018).
50. Behan, F. M. et al. Prioritization of cancer therapeutic targets using CRISPR-Cas9 screens. *Nature* **568**, 511–516 (2019).
51. Boehm, J. S. et al. Cancer research needs a better map. *Nature* **589**, 514–516 (2021).
52. Iorio, F. et al. A landscape of pharmacogenomic interactions in cancer. *Cell* **166**, 740–754 (2016).
53. Amaravadi, R. K., Kimmelman, A. C. & Debnath, J. Targeting autophagy in cancer: recent advances and future directions. *Cancer Discov.* **9**, 1167–1181 (2019).
54. Meehan, T. F. et al. PDX-MI: Minimal information for patient-derived tumor xenograft models. *Cancer Res.* **77**, e62–e66 (2017).
55. Koc, S. et al. PDXNet portal: patient-derived xenograft model, data, workflow and tool discovery. *NAR Cancer* **4**, zcac014 (2022).
56. Meric-Bernstam, F. et al. Assessment of patient-derived xenograft growth and antitumor activity: the NCI PDXNet consensus recommendations. *Mol. Cancer Ther.* **23**, 924–938 (2024).
57. Guillen, K. P. et al. A human breast cancer-derived xenograft and organoid platform for drug discovery and precision oncology. *Nat. Cancer* **3**, 232–250 (2022).
58. Ooft, S. N. et al. Prospective experimental treatment of colorectal cancer patients based on organoid drug responses. *ESMO Open* **6**, 100103 (2021).
59. Bakula, D. et al. WIPI3 and WIPI4 β -propellers are scaffolds for LKB1-AMPK-TSC signalling circuits in the control of autophagy. *Nat. Commun.* **8**, 15637 (2017).
60. Lee, J. Y. et al. HDAC6 controls autophagosome maturation essential for ubiquitin-selective quality-control autophagy. *EMBO J.* **29**, 969–980 (2010).

61. Hogenson, T. L. et al. Culture media composition influences patient-derived organoid ability to predict therapeutic responses in gastrointestinal cancers. *JCI Insight* **7**, e158060 (2022).
62. Dijkstra, K. K. et al. Generation of tumor-reactive T cells by co-culture of peripheral blood lymphocytes and tumor organoids. *Cell* **174**, 1586–1598.e12 (2018).
63. Strating, E. et al. Co-cultures of colon cancer cells and cancer-associated fibroblasts recapitulate the aggressive features of mesenchymal-like colon cancer. *Front. Immunol.* **14**, 1053920 (2023).
64. Farin, H. F. et al. Colorectal cancer organoid-stroma biobank allows subtype-specific assessment of individualized therapy responses. *Cancer Discov.* **13**, 2192–2211 (2023).
65. Neal, J. T. et al. Organoid modeling of the tumor immune micro-environment. *Cell* **175**, 1972–1988.e16 (2018).
66. Voabil, P. et al. An ex vivo tumor fragment platform to dissect response to PD-1 blockade in cancer. *Nat. Med.* **27**, 1250–1261 (2021).
67. Dunne, P. D. et al. Cancer-cell intrinsic gene expression signatures overcome intratumoural heterogeneity bias in colorectal cancer patient classification. *Nat. Commun.* **8**, 15657 (2017).
68. Van der Auwera, G. A. et al. From FastQ data to high confidence variant calls: the Genome Analysis Toolkit best practices pipeline. *Curr. Protoc. Bioinform.* **43**, 11.10.1–11.10.33 (2013).
69. Nakken, S. et al. Personal Cancer Genome Reporter: variant interpretation report for precision oncology. *Bioinformatics* **34**, 1778–1780 (2018).
70. Kent, W. J. BLAT-the BLAST-like alignment tool. *Genome Res.* **12**, 656–664 (2002).
71. Scheinin, I. et al. DNA copy number analysis of fresh and formalin-fixed specimens by shallow whole-genome sequencing with identification and exclusion of problematic regions in the genome assembly. *Genome Res.* **24**, 2022–2032 (2014).
72. Dobin, A. et al. STAR: ultrafast universal RNA-seq aligner. *Bioinformatics* **29**, 15–21 (2013).
73. Tarasov, A., Vilella, A. J., Cuppen, E., Nijman, I. J. & Prins, P. Sambamba: fast processing of NGS alignment formats. *Bioinformatics* **31**, 2032–2034 (2015).
74. Wang, L., Wang, S. & Li, W. RSeQC: quality control of RNA-seq experiments. *Bioinformatics* **16**, 2184–2185 (2012).
75. Liao, Y., Smyth, G. K. & Shi, W. featureCounts: an efficient general purpose program for assigning sequence reads to genomic features. *Bioinformatics* **30**, 923–930 (2014).
76. Love, M. I., Huber, W. & Anders, S. Moderated estimation of fold change and dispersion for RNA-seq data with DESeq2. *Genome Biol.* **15**, 550 (2014).
77. Wu, T. et al. clusterProfiler 4.0: a universal enrichment tool for interpreting omics data. *Innovation* **2**, 100141 (2021).
78. Yu, G., Wang, L. G., Han, Y. & He, Q. Y. clusterProfiler: an R package for comparing biological themes among gene clusters. *OMICS* **16**, 284–287 (2012).
79. Yu, G., Wang, L. G., Yan, G. R. & He, Q. Y. DOSE: an R/Bioconductor package for disease ontology semantic and enrichment analysis. *Bioinformatics* **31**, 608–609 (2015).
80. Subramanian, A. et al. Gene set enrichment analysis: a knowledge-based approach for interpreting genome-wide expression profiles. *Proc. Natl Acad. Sci. USA* **102**, 15545–15550 (2005).
81. Supek, F., Bošnjak, M., Škunca, N. & Šmuc, T. REVIGO summarizes and visualizes long lists of gene ontology terms. *PLoS ONE* **6**, e21800 (2011).
82. Eide, P. W., Bruun, J., Lothe, R. A. & Sveen, A. CMScaller: an R package for consensus molecular subtyping of colorectal cancer pre-clinical models. *Sci. Rep.* **7**, 16618 (2017).
83. Baralis, E., Bertotti, A., Fiori, A. & Grand, A. LAS: a software platform to support oncological data management. *J. Med. Syst.* **36**, S81–S90 (2012).
84. Schindelin, J. et al. Fiji: an open-source platform for biological-image analysis. *Nat. Methods* **9**, 676–682 (2012).
85. Mölder, F. et al. Sustainable data analysis with Snakemake. *F1000Research* **10**, 33 (2021).

Acknowledgements

We acknowledge Merck KGaA for providing cetuximab. We thank Mauro Papotti, Gianluca Paraluppi, and Serena Perotti for sample acquisition; Alessandro Fiori and Massimiliano Frassà for data management; Massenzio Fornasier and Arianna Russo for veterinary assistance; Fabrizio Maina for animal husbandry; Raffaella Albano, Lara Fontani, Stefania Giove, and Laura Palmas for technical assistance; and Daniela Gramaglia and Mauro Paschetta for secretarial assistance. This work was conducted with funding from AIRC, Associazione Italiana per la Ricerca sul Cancro, Investigator Grants 20697 (to A.B.), 22802 (to L.T.), and 23211 (to L.P.); AIRC 5×1000 grant 21091 (to A.B. and L.T.); AIRC/CRUK/FC AECC Accelerator Award 22795 (to L.T.); AIRC MFAG 25040 (to A.P.); European Research Council Consolidator Grant 724748 BEAT (to A.B.); H2020 grant agreement no. 754923 COLOSSUS (to L.T.); H2020 INFRAIA grant agreement no. 731105 EDIREX (to A.B.); Horizon Europe grant agreement no. 101058620 canSERV (to L.T.); Italian Ministry of University and Research, National Recovery and Resilience Plan, project PNC0000001 (to L.T.); Fondazione Piemontese per la Ricerca sul Cancro-ONLUS, 5×1000 Ministero della Salute 2016 (to L.T.); and Ricerca Finalizzata 2021 Giovani Ricercatori, ID. GR-2021-12375316 (to E.G.). A.B. and L.T. are members of the EurOPDX Consortium.

Author contributions

S.M.L. and E.G. designed the study, interpreted the data, and contributed to manuscript writing. M.A. performed the CRISPR-Cas9-based *EGFR* gene editing experiments with tumoroids. V.V., F.C., B.L., I.C., M.P., and L.S. performed pharmacologic experiments with tumoroids under the supervision of S.M.L. L.d.B., D.S., and M.V.M. performed pharmacologic experiments with tumoroids under the supervision of A.P. and L.P. M.F., S.B., G.C., and M.V. analyzed molecular data under the supervision of E.G. V.V., F.C., E.R.Z., and F.S. conducted drug efficacy studies in mice. F.G. generated and coordinated the biobank of molecular derivatives from patient samples. E.R.Z., A.M., A.F., and C.C.Z. procured patient samples and collected clinical metadata. A.B. and L.T. designed the research and interpreted results, supervised and coordinated the study and wrote the paper. All authors critically reviewed, edited, and approved the final version of the manuscript.

Competing interests

L.T. has received research grants from Menarini, Merck KGaA, Merus, Pfizer, Servier, and Symphogen. The other authors declare no conflicts.

Additional information

Supplementary information The online version contains supplementary material available at <https://doi.org/10.1038/s41467-024-51909-2>.

Correspondence and requests for materials should be addressed to Andrea Bertotti or Livio Trusolino.

Peer review information *Nature Communications* thanks the anonymous reviewer(s) for their contribution to the peer review of this work. A peer review file is available.

Reprints and permissions information is available at <http://www.nature.com/reprints>

Publisher's note Springer Nature remains neutral with regard to jurisdictional claims in published maps and institutional affiliations.

Open Access This article is licensed under a Creative Commons Attribution-NonCommercial-NoDerivatives 4.0 International License, which permits any non-commercial use, sharing, distribution and reproduction in any medium or format, as long as you give appropriate credit to the original author(s) and the source, provide a link to the Creative Commons licence, and indicate if you modified the licensed material. You do not have permission under this licence to share adapted material derived from this article or parts of it. The images or other third party material in this article are included in the article's Creative Commons licence, unless indicated otherwise in a credit line to the material. If material is not included in the article's Creative Commons licence and your intended use is not permitted by statutory regulation or exceeds the permitted use, you will need to obtain permission directly from the copyright holder. To view a copy of this licence, visit <http://creativecommons.org/licenses/by-nc-nd/4.0/>.

© The Author(s) 2024